A: Kinetics, Dynamics, Photochemistry, and Excited States

Acetonyl Peroxy and Hydro Peroxy Self- and Cross-Reactions: Kinetics, Mechanism, and Chaperone Enhancement from the Perspective of the Hydroxyl Radical Product

Kristen Zuraski, Aileen O. Hui, Fred J. Grieman, Emily Darby, Kristian H. Møller, Frank A. F. Winiberg, Carl J. Percival, Matthew D. Smarte, Mitchio Okumura, Henrik Grum Kjaergaard, and Stanley P Sander

J. Phys. Chem. A, **Just Accepted Manuscript** • DOI: 10.1021/acs.jpca.0c06220 • Publication Date (Web): 27 Aug 2020

Acetonyl Peroxy and Hydro Peroxy Self- and Cross- Reactions: Kinetics, Mechanism, and Chaperone Enhancement from the Perspective of the Hydroxyl Radical Product

Kristen Zuraski,[a] Aileen O. Hui,[b,c] Fred J. Grieman,[*,a,d] Emily Darby,[a,d,e] Kristian H. Møller,[f] Frank A. F. Winiberg,[a] Carl J. Percival,[a] Matthew D. Smarte,[b] Mitchio Okumura,[b] Henrik G. Kjaergaard,[*,f] and Stanley P. Sander[*,a]

[a]NASA Jet Propulsion Laboratory, California Institute of Technology, 4800 Oak Grove Drive, Pasadena, California 91109, United States

[b]Arthur Amos Noyes Laboratory of Chemical Physics, California Institute of Technology, Pasadena, California 91125, United States

[c]now at: The Aerospace Corporation, El Segundo, California 90245, United States`

[d]Seaver Chemistry Laboratory, Pomona College, Claremont, California 91711, United States

[e]now at: Trussell Technologies, Oakland, California 94612, United States

[f]Department of Chemistry, University of Copenhagen, Universitetsparken 5, DK-2100 Copenhagen Ø, Denmark

Corresponding Authors
*fjg04747@pomona.edu (F.J.G); hgk@chem.ku.dk (H.G.K); stanley.p.sander@jpl.nasa.gov (S.P.S.).

ABSTRACT

Pulsed laser photolysis coupled with infrared (IR) wavelength modulation spectroscopy and ultraviolet (UV) absorption spectroscopy was used to study the kinetics and branching fractions for the acetonyl peroxy ($CH_3C(O)CH_2O_2$) self-reaction and its reaction with hydro peroxy (HO_2) at a temperature of 298 K and pressure of 100 Torr. Near-IR and mid-IR lasers simultaneously monitored HO_2 and hydroxyl, OH, respectively, while UV absorption measurements monitored the $CH_3C(O)CH_2O_2$ concentrations. The overall rate constant for the reaction between $CH_3C(O)CH_2O_2$ and HO_2 was found to be $(5.5 \pm 0.5) \times 10^{-12}$ cm^3 molecule^{-1} s^{-1} and the branching fraction for OH yield from this reaction was directly measured as 0.30 ± 0.04. The $CH_3C(O)CH_2O_2$ self-reaction rate constant was measured to be $(4.8 \pm 0.8) \times 10^{-12}$ cm^3 molecule^{-1} s^{-1} and the branching fraction for alkoxy formation was inferred from secondary chemistry as 0.33 ± 0.13. An increase in the rate of the HO_2 self-reaction was also observed as a function of acetone ($CH_3C(O)CH_3$) concentration which is interpreted as a chaperone effect resulting from hydrogen-bond complexation between HO_2 and $CH_3C(O)CH_3$. The chaperone enhancement coefficient for $CH_3C(O)CH_3$ was determined to be $k''_A = (4.0 \pm 0.2) \times 10^{-29}$ cm^6 molecule^{-2} s^{-1} and the equilibrium constant for $HO_2 \bullet CH_3C(O)CH_3$ complex formation was found to be K_c(R15) $= (2.0 \pm 0.89) \times 10^{-18}$ cm^3 molecule^{-1}; from these values the rate constant for the HO_2 + $HO_2 \bullet CH_3C(O)CH_3$ reaction was estimated to be $(2 \pm 1) \times 10^{-11}$ cm^3 molecule^{-1} s^{-1}. Results from UV absorption cross-section measurements of $CH_3C(O)CH_2O_2$ and prompt OH radical yields arising from possible oxidation of the $CH_3C(O)CH_3$-derived alkyl radical are also discussed. Using theoretical methods, no likely pathways for the observed prompt OH radical formation have been found and thus remains unexplained.

I. INTRODUCTION

Atmospheric oxidation of volatile organic compounds (VOCs, RH) leads to the formation of organic peroxy radicals, RO_2. These species play a vital role in the budgets of O_3, NO_x ($NO + NO_2$), NO_y ($NO_x + NO_z$; $NO_z = HNO_3$, HONO, PAN + other nitrogen oxides), and HO_x ($OH + HO_2$) throughout the troposphere and, consequently, are important in determining atmospheric composition, the Earth's radiative balance and future changes in climate. Once formed, RO_2 can react with NO_x, HO_2 (R1), OH, other R'O_2 species/itself (R2), or undergo H-shift reactions to form autoxidation products (R3) as shown in Figure 1.[1-10]

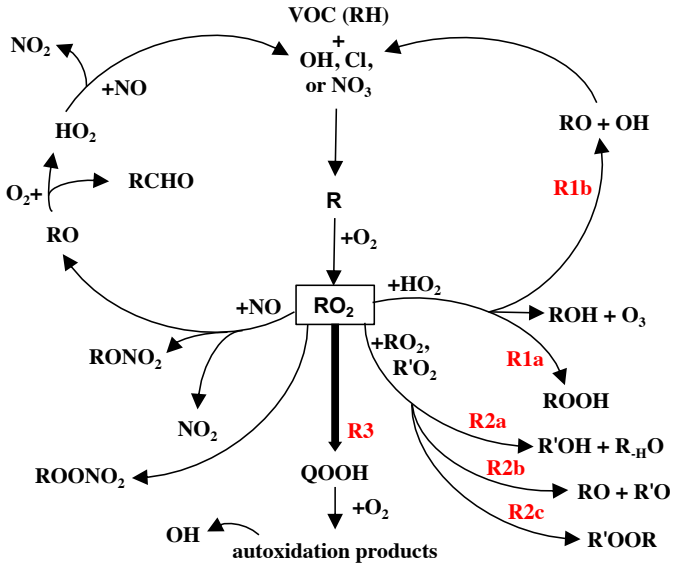

Figure 1. General scheme for RO_2 chemistry in the atmosphere.[1, 2] The right and left side represent low and high NO_x environments, respectively. The bold arrow indicates unimolecular rearrangement by H-shift reactions.

In pristine environments, direct emissions from vegetation, oxidation of anthropogenic and biogenic hydrocarbons, oceans, and biomass burning make acetone, $CH_3C(O)CH_3$, one of the most abundant oxygenated VOCs in the atmosphere.[11-14] Following oxidation of $CH_3C(O)CH_3$ to form acetonyl peroxy, $CH_3C(O)CH_2O_2$, reactions with hydro peroxy, HO_2, dominate in low NO_x environments and impact the HO_x balance by removing HO_2 and working as either a HO_x radical sink through the formation of hydroperoxides (ROOH, R1a) or as radical

propagation by generating hydroxyl radicals (OH, R1b).[15-21] The ozone generating pathway shown in Figure 1 is not available for $CH_3C(O)CH_2O_2$ due to the position of the carbonyl group.[16]

$$HO_2 + CH_3C(O)CH_2O_2 \rightarrow CH_3C(O)CH_2OOH + O_2 \quad \text{(R1a)}$$

$$\rightarrow CH_3C(O)CH_2O + OH + O_2 \quad \text{(R1b)}$$

The importance of accurately accounting for the OH production from peroxy radical reactions (R1b, in Fig. 1) is driven in part by OH field measurements in pristine environments which report elevated mixing ratios compared with atmospheric models.[22-25] OH-recycling from peroxy radical reactions as well as autoxidation reactions may explain, in part, the discrepancy between measurements and models.

Additional fates of the $CH_3C(O)CH_2O_2$ radical in pristine environments include reactions with other peroxy radicals and with itself. These reactions are less dominating in the atmosphere compared to reactions with NO_x and HO_2, but are important for laboratory studies. Similar to other peroxy radicals, there are two established self-reaction pathways for $CH_3C(O)CH_2O_2$: one which leads to hydroxyacetone ($CH_3C(O)CH_2OH$) and methylglyoxal ($CH_3C(O)CHO$) as stable products (R2a) and the other that generates acetonoxy radical ($CH_3C(O)CH_2O$, R2b).[21, 26, 27] In addition, a third pathway, R2c, was recently proposed and observed by Berndt et al., which leads to higher functionalized accretion products, ROOR.[28]

$$2\ CH_3C(O)CH_2O_2 \rightarrow CH_3C(O)CH_2OH + CH_3C(O)CHO + O_2 \quad \text{(R2a)}$$

$$\rightarrow 2\ CH_3C(O)CH_2O + O_2 \quad \text{(R2b)}$$

$$\rightarrow C_6H_{10}O_4 + O_2\ (\text{ROOR}) \quad \text{(R2c)}$$

Previously, the cross-reaction rate constant for $CH_3C(O)CH_2O_2 + HO_2$ (k_1) has only been measured once by Bridier et al.[21] using flash photolysis and ultraviolet (UV) absorption of

$CH_3C(O)CH_2O_2$ and other radicals. As with all spectroscopic studies, the experimentally determined rate constant is highly sensitive to the values of the UV absorption cross-sections employed. However, the reported literature values of UV absorption cross-section for $CH_3C(O)CH_2O_2$ radical, $\sigma_{CH3C(O)CH2O2}$, are not in good agreement and vary by up to a factor of 2.5.[21, 26, 29] The k_1 rate constant from the Bridier et al.[21] study was determined using much larger $\sigma_{CH3C(O)CH2O2}$ values compared to other literature works. In subsequent studies, their value for k_1 was used to determine the branching fraction for OH formation,[15, 18-20] which propagated any error in their reported k_1 to the reported branching fraction values. The literature values for the branching fraction of the OH generating channel, k_{1b}/k_1, are not in agreement, ranging from 0.15 – 0.67. A single theoretical study by Hasson et al.[16] of the branching between R1a and R1b finds that R1a is favored, but lowering the energy of the $CH_3C(O)CH_2O_2 \bullet HO_2$ intermediate complex by just 2 kcal mol^{-1} inverts the branching to favor R1b demonstrating the sensitivity of the branching fraction to the energies determined in the structure calculations. None of these experimental or theoretical studies have considered H-shift isomerization reactions.

The rate constant for the $CH_3C(O)CH_2O_2$ self-reaction (k_2) has been measured by two studies[21, 26] that are in agreement but with one only reporting an upper limit[26]. This agreement may be fortuitous, however, because significantly different $\sigma_{CH3C(O)CH2O2}$ were used between these two studies. Subsequent indirect observation of the branching fraction of k_{2b}/k_2 by Emricha and Warneck[30] did not agree with the results by Bridier et al.[21] showing a difference of 0.25. The most recent results by Berndt et al.[28] measured k_{2c} only and based the branching fraction for this channel on the results of the previous studies.

Our work is the first study to monitor simultaneously the time-dependent concentration profiles for $CH_3C(O)CH_2O_2$, HO_2, and OH independently. The goal of this work is to reassess

and resolve the discrepancies in the overall kinetic rate constants, k_1 and k_2, and the associated branching fractions. We have re-measured $\sigma_{CH3C(O)CH2O2}$ at selected wavelengths in the region between 290 – 320 nm and constrained the results of our kinetic model fits by coupling the kinetic data of $CH_3C(O)CH_2O_2$ with HO_2 and OH, both obtained through infrared wavelength modulated spectroscopy (IR-WMS). In addition, a significant chaperone effect caused by $CH_3C(O)CH_3$ forming a hydrogen-bonded (H-bonded) complex with HO_2 that, in turn, increases the HO_2 self-reaction rate was also observed at room temperature and is reported here for the first time. This HO_2 self-reaction rate enhancement must be included in the analysis to obtain accurate kinetic parameters for the $CH_3C(O)CH_2O_2$ chemistry.

II. METHODS

IIa. Experimental

Infrared Kinetic Spectroscopy (IRKS)

Experiments conducted using the Infrared Kinetic Spectroscopy (IRKS) apparatus to study peroxy radical chemistry have been reported in earlier publications.[31-33] Therefore, the method is discussed only briefly here with an emphasis on improvements in the detection capabilities and details specific to this work. The general schematic is shown in Figure 2.

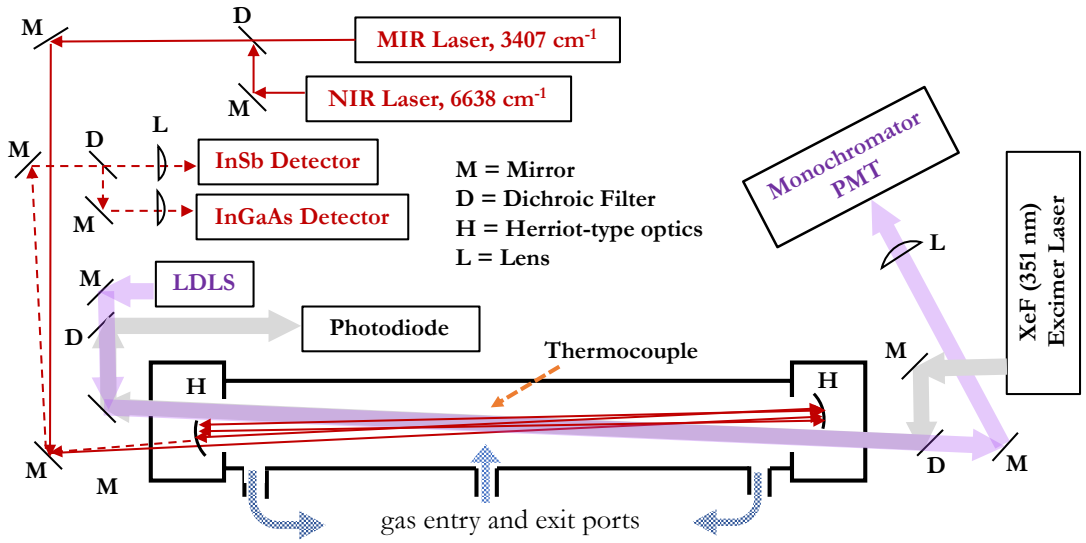

Figure 2. Experimental schematic of the IRKS apparatus. M, D, H, and L are mirrors, dichroic filters, half-moon shaped Herriott mirrors, and lenses, respectively. The Herriott mirrors are housed inside nitrogen purged boxes attached to the jacketed cell. Solid Red lines represent the IR beam paths prior to entering the cell, the reflecting red lines in the cell represent thirty passes in a Herriott optic geometry, and the dashed red lines represent the IR beam paths after exiting the cell. The laser driven UV light source (LDLS) and 351 nm photolysis laser counter-propagated the cell entering/exiting the cell at a height offset but crossing the IR beam paths.

Pulsed laser photolysis (PLP) by a XeF excimer laser (Lambda Physik Compex 301, 351 nm, 110 mJ/pulse in constant energy mode, 0.2 Hz repetition rate) was used to initiate reactions in a continuous, temperature-controlled (T = 298 ± 1 K) flow cell (175 cm long, 5 cm diameter). The repetition rate of the photolysis laser was set to ensure products diffused out of the reaction volume between pulses and the flow cell pressure and temperature were held constant at 100 Torr and 298 K, respectively. Collimated broadband UV light generated by a laser driven light source (LDLS, Energetiq EQ-99XFC) counter propagated the excimer beam path through the cell and was separated from the excimer beam by a dichroic mirror and dispersed using a monochromator (Acton Research Corporation Spectra Pro-300i, slit width ~160 μm) coupled to a photomultiplier tube (EMI 9781A) for UV absorption measurements. The gas exit port positions (located in front of the Herriott mirrors, as shown in Figure 2) dictated the UV absorption

pathlength, which was measured to be 148 ± 10 cm long by Cl_2 absorption at 320 nm (σ_{Cl2} = 2.37×10^{-19} cm^2).[31]

Two continuous-wave distributed feedback IR lasers (NASA JPL Microdevices Laboratory), were each wavelength modulated at 6.8 MHz, entered the cell through a hole in a custom coated mirror (Rocky Mountain Instrument Co.) aligned in a Herriott optical arrangement to achieve thirty passes through the cell, resulting in a total IR effective path length of approximately 27 m for each laser.[34] The Herriott mirrors were mounted inside nitrogen purged boxes attached to both ends of the cell as shown in Figure 2. After exiting the cell, the IR signals were detected independently using an indium gallium arsenide detector (InGaAs, New Focus 1811) and a liquid nitrogen-cooled indium antimonide detector (InSb, Infrared Associates IS-0.25) for the near- and mid-IR light, respectively. These signals were demodulated at 13.6 MHz and amplified by a factor of 200 for 2*f*-heterodyne detection. Similar to previous works,[31-33] the concentrations derived from the 2*f* signals for both lasers detection axes were calibrated daily (See SI for details.).

In a typical experiment, the time-dependent UV absorption trace and the two IR kinetic traces were recorded simultaneously following the excimer photolysis pulse. Typical datasets comprised all three signals that were digitized and averaged for 800 excimer shots while simultaneously being recorded using NI LabVIEW software.

Chemicals and Radical Generation

Measured flows of nitrogen carrier gas (N_2, Airgas Corps., 99.997%) were bubbled through methanol (CH_3OH, Fisher Optima A454-1, >99.9%) and acetone ($CH_3C(O)CH_3$, Fisher Optima A929-1, >99.9%) to entrain these species in the gas phase. Changes in the bubbler flow rates were used to vary the concentrations of gaseous CH_3OH and $CH_3C(O)CH_3$. These

precursor gases were combined and premixed in a temperature-controlled glass manifold with chlorine (Cl_2, Air Products, 9.99% in He), oxygen (O_2, Airgas Corps., 99.996%), and N_2 (Airgas Corps., 99.997%) and then introduced through a central port of the flow cell (at the same temperature) depicted in Figure 2. Individual flow rates of the reaction precursors and the nitrogen bath gas were controlled using mass flow controllers (MKS Instruments). The total flow rate was 2160 sccm and the flow cell residence time was 9.7 s.

Photolysis of Cl_2 by pulsed 351 nm light generated atomic chlorine, Cl, to initiate reactions with $CH_3C(O)CH_3$ (R4) and CH_3OH (R6) to generate $CH_3C(O)CH_2O_2$ (R5) and HO_2 (R7), respectively, in the presence of O_2.

$$CH_3C(O)CH_3 + Cl \rightarrow CH_3C(O)CH_2 + HCl \quad (R4)$$

$$CH_3C(O)CH_2 + O_2 (+M) \rightarrow CH_3C(O)CH_2O_2 \quad (R5)$$

$$CH_3OH + Cl \rightarrow CH_2OH + HCl \quad (R6)$$

$$CH_2OH + O_2 \rightarrow HO_2 + CH_2O \quad (R7)$$

Typical initial concentrations for investigating the cross-reaction, R1, averaged $[Cl_2] = 9 – 10 \times 10^{15}$, $[Cl]_0 = 1 – 2 \times 10^{14}$, $[CH_3OH] = 4 \times 10^{15}$, $[CH_3C(O)CH_3] = 1.7 – 2.8 \times 10^{16}$, and $[O_2] = 1.6 \times 10^{18}$ molecule cm^{-3} with N_2 added to achieve the total pressure. Concentrations of the precursors for observing R1 were set to have ratios of $[HO_2]/[CH_3C(O)CH_2O_2]$ between 4 – 6 to keep HO_2 in excess of $CH_3C(O)CH_2O_2$ to reduce secondary chemistry from the $CH_3C(O)CH_2O_2$ self-reaction. Similar initial concentrations in the absence of CH_3OH were used for the UV cross-section measurements and for investigating R2.

Detection of Key Species

Combining the UV absorption and IR-WMS techniques makes this the first study to simultaneously monitor the time-dependent concentrations of $CH_3C(O)CH_2O_2$, HO_2, and OH

radicals. $CH_3C(O)CH_2O_2$ concentrations were detected by UV absorption spectroscopy using 312 nm light. At the same time, IR-WMS was used to monitor concentrations of HO_2 and the product OH at 6638.2 and 3407.6 cm^{-1}, respectively, via ro-vibrational lines. Under these experimental conditions, the normalized noise-equivalent sensitivity concentrations for the detection of HO_2 and OH radicals were on the order of 10^8 molecule cm^{-3} $Hz^{-1/2}$ (10^9 molecule cm^{-3} for typical experiments).

IIb. Kinetic Modeling for Fitting Experimental Data

Because of the large number of reactions involved, numerical chemical simulations were necessary for extracting quantitative results for the rate constants and branching fractions of R1 and R2. A Python code adapted from an existing library[35] was used as a numerical integrator and fitting software encompassing the comprehensive mechanism shown in Table 1. The reaction list was constructed from a combination of the reactions listed in the JPL Data Evaluation 15-10 and relevant papers.[18, 33, 36] $CH_3C(O)CH_2O_2$, HO_2, and OH kinetic data were fit simultaneously using a Levenberg-Marquardt algorithm[37, 38] to optimize the kinetic rate constants and branching fractions against the datasets. Weights were applied to equalize the fitting across the different magnitudes of species concentrations. The fits were iterated 1000 times per experimental run following a Monte Carlo (MC) algorithm to randomly sample all parameters and systematic uncertainties (reaction rate constants and branching fractions, concentrations, calibration constants, the cell pathlength, Poisson counting in the data, and absorption cross sections) within each respective uncertainty. Initial guesses for the fitted parameters were sampled manually to ensure local minima were avoided. This procedure resulted in distributions of each fitted parameter from which its mean and uncertainty (reported as 1σ unless otherwise stated) could then be determined.

The self-reaction data (R2) was analyzed first. Here, OH and HO_2 kinetics are the result of secondary chemistry that is directly affected by the overall kinetic rate of R2 and the branching fraction R2b/R2 (discussed in section IIIb). The resulting fits determined the overall rate constant k_2 and the branching fraction, k_{2b}/k_2. In order to determine the rate constant and branching fraction for the cross-reaction, R1, the results of fitting R2 were incorporated into the model, and the experimental concentrations were set to minimize contributions from R2 by keeping HO_2 in excess of $CH_3C(O)CH_2O_2$ ($[HO_2]/[CH_3C(O)CH_2O_2] > 4$). The sensitivity of the model for the cross-reaction to the rate of the self-reaction was tested and found to be negligible for the range $k_2 = 3.5 – 6.0 \times 10^{-12}$ cm^3 molecule^{-1} s^{-1} under the conditions used in this work. The three $[CH_3C(O)CH_2O_2]$, $[HO_2]$ and [OH] time-dependent datasets were again fit simultaneously. For experimental runs of R1, the fitted parameters included k_{1a}, k_{1b}, and the chaperone enhanced HO_2 self-reaction rate constant, $k_{12,obs}$ (sections IIIb and IIIc). Following the determination of the fit parameters for the cross-reaction, these values were used to re-run the MC simulations for the self-reaction data to verify that the final values of k_2 and k_{2b}/k_2 were unaffected by the change in k_{1a}, k_{1b}, and $k_{12,obs}$.

Table 1. Reaction scheme used in the determination of rates, branching fractions, and chaperone effects for the self- and cross- reactions of $CH_3C(O)CH_2O_2$ and HO_2. Rate constants are taken from the JPL Data Evaluation 15-10 recommended values[36] and are all in cm^3 molecule^{-1} s^{-1}, unless indicated otherwise. Uncertainties in values are given in their respective references.

k	Reaction	Branching Ratio	Rate Constant	Ref.
	Initial Radical Reactant Generation			
k_6	$CH_3OH + Cl \rightarrow CH_2OH + HCl$		5.5×10^{-11}	
k_7	$CH_2OH + O_2 \rightarrow HO_2 + CH_2O$		9.1×10^{-12}	
k_4	$CH_3C(O)CH_3 + Cl \rightarrow CH_3C(O)CH_2 + HCl$		$1.63 \times 10^{-11} \exp(-610/T)$	
k_{5a}	$CH_3C(O)CH_2 + O_2 (+M) \rightarrow CH_3C(O)CH_2O_2$	0.98	2.75×10^{-31}[M]	
k_{5b}	$CH_3C(O)CH_2 + O_2 (+M) \rightarrow OH + products$	0.01		
k_{5c}	$CH_3C(O)CH_2 + O_2 (+M) \rightarrow HO_2 + products$	0.01		

	Primary Chemistry			
k_{12}	$HO_2 + HO_2 \rightarrow H_2O_2 + O_2$		$1.5 \times 10^{-12} + 4.0 \times 10^{-29} \times [CH_3C(O)CH_3]$	*this work*
k_{2a}	$2CH_3C(O)CH_2O_2 \rightarrow CH_3C(O)CHO + CH_3C(O)CH_2OH + O_2$		4.8×10^{-12}	*this work*
k_{2b}	$2CH_3C(O)CH_2O_2 \rightarrow 2\ CH_3C(O)CH_2O + O_2$	0.68		
k_{2c}	$2CH_3C(O)CH_2O_2 \rightarrow$ accretion products			
k_{1a}	$HO_2 + CH_3C(O)CH_2O_2 \rightarrow CH_3C(O)CH_2OOH + O_2$	0.70	5.5×10^{-12}	*this work*
k_{1b}	$HO_2 + CH_3C(O)CH_2O_2 \rightarrow CH_3C(O)CH_2O + OH + O_2$	0.30		
	Secondary Chemistry			
	$OH + CH_3OH \rightarrow CH_2OH + H_2O$	0.85	2.9×10^{-12} exp(-345/T)	
	$OH + CH_3OH \rightarrow CH_3O + H_2O$	0.15		
	$OH + CH_3C(O)CH_3 \rightarrow H_2O + CH_3COCH_2$	0.98	$1.33 \times 10^{-13} + 3.82 \times 10^{-11} \times$ exp(-2000/T)	
	$OH + CH_3C(O)CH_3 \rightarrow CH_3 + CH_3COOH$	0.02		
k_{11}	$Cl + HO_2 \rightarrow OH + ClO$		3.6×10^{-11} exp(-375/T)	
	$Cl + HO_2 \rightarrow O_2 + HCl$		1.4×10^{-11} exp(270/T)	
	$2\ CH_3O_2 \rightarrow 2\ CH_3O + O_2$	0.59	3.5×10^{-13}	
	$2\ CH_3O_2 \rightarrow CH_3OH + CH_2O + O_2$	0.41		
	$HO_2 + CH_3O_2 \rightarrow CH_3OOH + O_2$	0.9	5.2×10^{-12}	
	$HO_2 + CH_3O_2 \rightarrow CH_2O + H_2O + O_2$	0.1		
	$OH + CH_3OOH \rightarrow$ products		3.8×10^{-12} exp(200/T)	
	$CH_3O + O_2 \rightarrow CH_2O + HO_2$		3.9×10^{-14} exp(-900/T)	
	$O + CH_2O \rightarrow$ products		3.4×10^{-11} exp(-1600/T)	
	$OH + CH_2O \rightarrow H_2O + HCO$		5.5×10^{-12} exp(125/T)	
	$HO_2 + CH_2O \rightarrow HOCH_2O_2$		6.7×10^{-15} exp(600/T)	
	$CH_3 + O_2$ (+M) $\rightarrow CH_3O_2$		1.16×10^{-31} [M]	
	$CH_3O_2 + CH_3C(O)CH_2O_2 \rightarrow CH_3C(O)CH_2O + CH_3O + O_2$	0.3	7.5×10^{-13} exp(500/T)	
	$CH_3O_2 + CH_3C(O)CH_2O_2 \rightarrow CH_3C(O)CH_2OH + CH_2O + O_2$	0.2		
	$CH_3O_2 + CH_3C(O)CH_2O_2 \rightarrow CH_3C(O)CHO + CH_3OH + O_2$	0.5		
k_{10}	$CH_3C(O)CH_2O + O_2 \rightarrow CH_3C(O)CHO + HO_2$		9.7×10^{-15}	39
k_8	$CH_3C(O)CH_2O \rightarrow CH_3CO + CH_2O$		rapid	39
	$OH + HO_2 \rightarrow H_2O + O_2$		4.8×10^{-11} exp(250/T)	
	$O + O_2$ (+M) $\rightarrow O_3$		6.10×10^{-24} [M]	
	$OH + HCl \rightarrow H_2O + Cl$		1.8×10^{-12} exp(-250/T)	
k_{9a}	$CH_3CO + O_2$ (+M) $\rightarrow CH_3C(O)O_2$	0.97	3.99×10^{-12}	40

k_{9b}	$CH_3CO + O_2 \rightarrow OH$ + products	0.01		
k_{9c}	$CH_3CO + O_2 \rightarrow HO_2$ + products	.02		
	$HO_2 + CH_3C(O)O_2 \rightarrow CH_3C(O)OOH + O_2$	0.29	1.72×10^{-11}	33
	$HO_2 + CH_3C(O)O_2 \rightarrow CH_3C(O)OH + O_3$	0.23		
	$HO_2 + CH_3C(O)O_2 \rightarrow OH + CH_3CO_2 + O_2$	0.48		
	$CH_3O_2 + CH_3C(O)O_2 \rightarrow CH_3CO_2 + CH_3O + O_2$	0.9	2.0×10^{-12} exp(500/T)	
	$CH_3O_2 + CH_3C(O)O_2 \rightarrow CH_3C(O)OH + CH_2O + O_2$	0.1		
	$CH_3CO_2 \rightarrow CH_3 + CO_2$		rapid	39
	$CH_3C(O)CH_2O_2 + CH_3C(O)O_2 \rightarrow CH_3C(O)CH_2O + CH_3CO_2 + O_2$	0.5	5.0×10^{-12}	21,41
	$CH_3C(O)CH_2O_2 + CH_3C(O)O_2 \rightarrow CH_3C(O)CHO + CH_3C(O)OH + O_2$	0.5		
	$2\ CH_3C(O)O_2 \rightarrow CH_3CO_2 + O_2 + CH_3CO_2$		2.9×10^{-12} exp(500/T)	
	$HOCH_2O_2 + HO_2 \rightarrow OH + O_2 + HOCH_2O$		5.6×10^{-15} exp(2300/T)	42, 43

IIc. THEORETICAL METHODS AND ENERGETICS

The potential for OH recycling via unimolecular reactions following O_2-addition to the acetonyl radical was modelled using a Rice-Ramsperger-Kassel-Marcus (RRKM) master equation (ME) approach reflecting the experimental conditions. The energetics are calculated as described in the approach by Møller et al.[44] and briefly outlined here. Conformers of reactants, transition states (TSs) and products are sampled using MMFF in Spartan '18 based on optimized structures at the B3LYP/6-31+G(d) level from Gaussian 16, rev. C.01.[45-52] For the transition states, suitable bond lengths are constrained in the conformer sampling. The resulting conformers are optimized at the B3LYP/6-31+G(d) level in Gaussian 16.[50] Unique conformers[44, 53] within 2 kcal mol^{-1} in electronic energy of the lowest energy conformer are further optimized at the ωB97X-D/aug-cc-pVTZ level[54-57] in Gaussian 16. For the conformer lowest in zero-point corrected electronic energy at this level, an RO-CCSD(T)-F12a/VDZ-F12 single-point calculation is done in Molpro2012.[58-63] The reactions are modelled using the Master Equation Solver for Multi Energy-well Reactions (MESMER)[63] based on the ωB97X-D/aug-cc-pVTZ thermodynamic properties of the lowest-energy conformers and improved using the RO-

CCSD(T)-F12a/VDZ-F12//ωB97X-D/aug-cc-pVTZ electronic energies. Further details of the MESMER modelling are given in the Supplemental Information (SI) Section SII. The rate coefficients for the unimolecular reactions of the thermalized species modelled are further calculated using the multi-conformer transition state theory (MC-TST) approach by Møller et al.[44] including the Eckart tunneling correction.[64] Rate coefficients of additional possible unimolecular reactions from subsequent intermediates were calculated at the same level of theory to aid the analysis of the experimental results (Section SIII in SI). All calculations are done at 298.15K.

III. RESULTS

IIIa. $CH_3C(O)CH_2O_2$ UV Absorption Cross-Section

The inset in Figure 3 displays a typical set of UV absorption data used to assess $\sigma_{CH3C(O)CH2O2}$ in the spectral region λ = 290 – 320 nm for select wavelengths (see SV in SI for complete data set). Experimental parameters were held constant as the monochromator grating position scanned across the spectral window in 5 nm steps. $CH_3C(O)CH_2O_2$ is a transient species, therefore, the reaction kinetics are coupled to quantifying $\sigma_{CH3C(O)CH2O2}$. Kinetic modeling was used to determine the time window for applying the fit at early times (0 – 2 ms) representative of second-order kinetics. The time window for the fit was optimized to exclude (1) scattered light and fluorescence from the excimer pulse which saturates the probe beam detector at early times (t < 0.2 ms), and (2) the influence of absorption from secondary species that absorb in this spectral region at later times (see SIV in SI for details). The inverse absorbance, 1/Abs, vs. time was used under the assumption of second-order analysis in this time range. The integrated rate law for second-order kinetics dictates that a linear fit corresponds to Equation 1

$$\frac{1}{Abs} = \frac{2k_2 t}{\sigma_{CH3C(O)CH2O2} l} + \frac{1}{[CH_3C(O)CH_2O_2]_0 \sigma_{CH3C(O)CH2O2} l} \quad [E1]$$

where l is the pathlength of the absorption measurement, k_2 is the bimolecular rate constant for R2, and $[CH_3C(O)CH_2O_2]_0$ is the initial concentration of $CH_3C(O)CH_2O_2$ formed at $t = 0$ s following reaction of the radical precursors. $[CH_3C(O)CH_2O_2]_0$ was equated with $[Cl]_0$ determined during the calibration experiments (see SI for details). In the absence of CH_3OH to form HO_2, the same initial concentration of $CH_3C(O)CH_2O_2$ forms under the condition of constant excimer power and $[Cl]_0$. The y-intercept from the linear fit was used to calculate the value of $\sigma_{CH3C(O)CH2O2}$ using E1. Our results are shown in Table 2 and Figure 4 with comparison to prior studies.[21, 26, 29, 36] The reported uncertainties were calculated through propagation of error and include the uncertainty in the linear fit, the pathlength, and the determined initial concentrations.

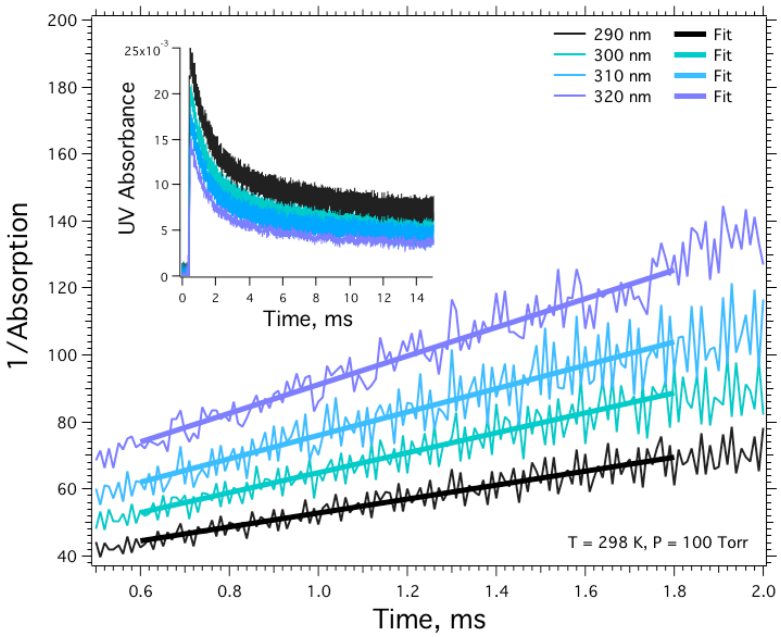

Figure 3. UV 1/Abs vs. time measurements obtained for $CH_3C(O)CH_3/Cl_2/O_2/N_2$ mixtures under conditions of constant laser power and $[Cl_2]$ to observe the $CH_3C(O)CH_2O_2$ self-reaction. Each UV time trace shown in the inset for selected wavelengths in the range $\lambda = 290 - 320$ nm was converted to 1/Abs and fit with a linear regression following second order kinetics in the 0.6 – 2 ms range. Additional datasets are shown in Figure S8 in the SI.

Table 2: Absorption cross-sections of $CH_3C(O)CH_2O_2$, $\sigma_{CH3C(O)CH2O2,}$ measured at T = 298 (±1) K and P = 100 (±1) Torr. Propagation of error for the reported uncertainties accounts for the uncertainties in the fits, pathlength, and initial radical concentrations.

λ (nm)	10^{20} σ (cm^2 $molecule^{-1}$)
290	212 (±38)
295	196 (±32)
300	192 (±31)
305	166 (±23)
310	164 (±22)
315	163 (±22)
320	141 (±17)

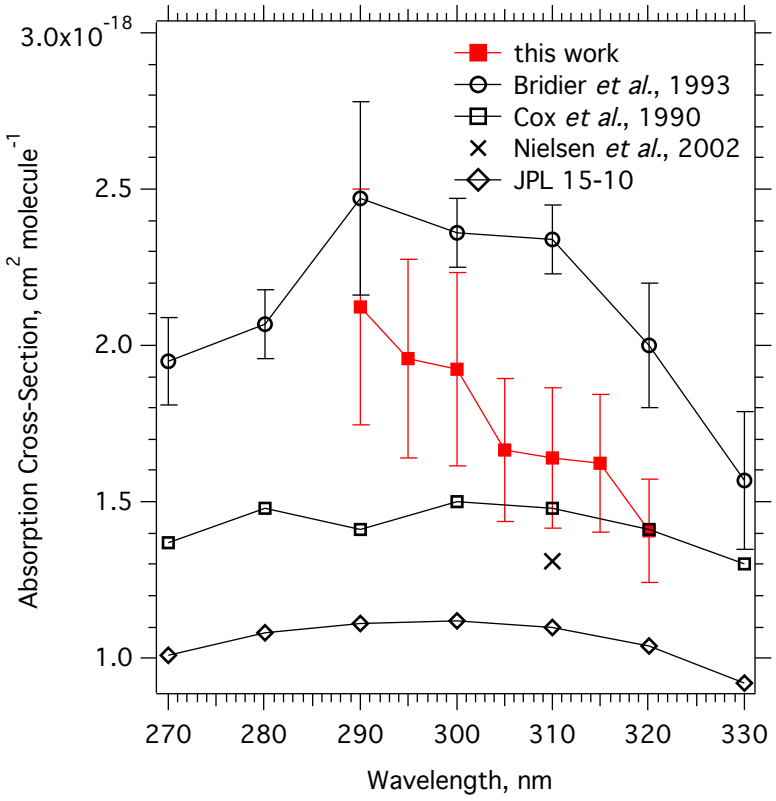

Figure 4. Comparison of the $CH_3C(O)CH_2O_2$ cross-section, $\sigma_{CH3C(O)CH2O2,}$ measured from this work (red squares), Bridier et al. (circles),[21] Cox et al. (squares),[26] Nielsen et al. (×),[29] and the recommended values by JPL Evaluation 15-10 (diamonds)[35] which reports the cross-section values from Cox et al. re-normalized to the absolute value at 240 nm measured by Nielsen et al. Errors in literature cross-section values were not available for all of the previous works as shown.

IIIb. $CH_3C(O)CH_2O_2$ self-reaction kinetics

Figure 5 shows comparisons between experimental data and the kinetic model using the IUPAC[66] recommended value of k_2, 8.0×10^{-12} cm^3 molecule^{-1} s^{-1}, vs. the value for k_2 determined from our MC simulations, 4.8×10^{-12} cm^3 molecule^{-1} s^{-1}. As is clearly seen, the recommended value for k_2 does not capture the $CH_3C(O)CH_2O_2$ kinetics observed in our experiments. Although Equation 1 could be used to determine the effective rate constant for R2 using the slope of the linear fit, it would result in large experimental uncertainty as a result of fitting only over a narrow temporal window. Fitting only $CH_3C(O)CH_2O_2$ would also leave determination of k_2 less constrained. To overcome these deficiencies, the concentration time profiles of HO_2 and OH were fit simultaneously with the $CH_3C(O)CH_2O_2$ radical kinetics using the MC simulation fitting method and model mechanism described in Section IIb and the absorption cross-sections given in Table 2. The time windows for the fits were 0.6 – 4, 0 – 20, and 0 – 2 ms for the $CH_3C(O)CH_2O_2$, HO_2, and OH kinetic traces, respectively, in order to disregard the early times for the UV data (<0.2 ms) that are affected by the excimer laser and data from later times to minimize higher contributions from secondary chemistry for each species.

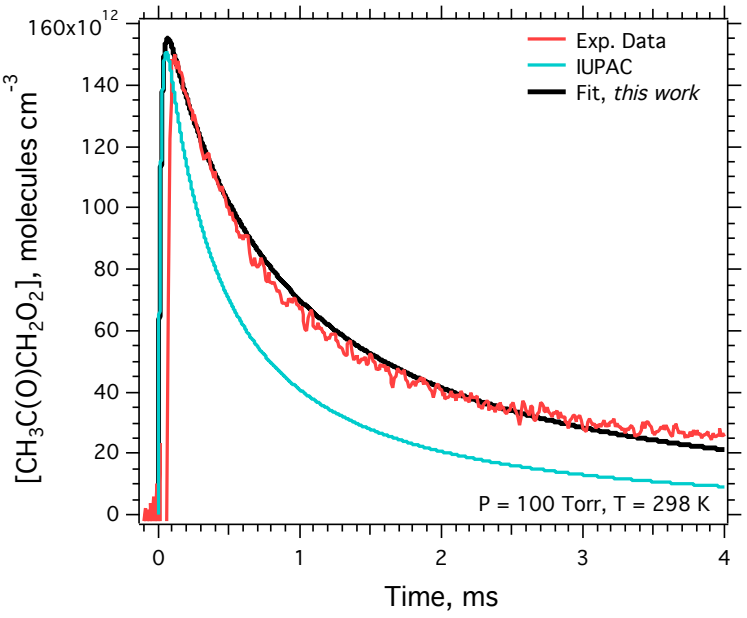

Figure 5. Experimental data (red) for [$CH_3C(O)CH_2O_2$] vs. time obtained by UV absorption measurements at 312 nm using linear interpolation of the 310 and 315 nm UV cross-sections determined in this work (Table 2). The kinetic simulation generated with recommended rate parameters for k_2 and k_{2b} / k_2 by IUPAC[66] is shown in turquoise and the fit from the MC simulations is shown in black.

Figure 6a and 6b show the experimental vs. simulated time-dependent HO_2 and OH concentrations, respectively, where the simulated kinetic profiles for each species using the IUPAC recommended values[66] are shown in turquoise. Results of this work, where k_2 and k_{2b} / k_2 were fit to the experimental data, are shown in black in Figure 6 and histograms representing the occurrences for the k_2 and k_{2b} / k_2 parameters from the MC simulations are shown in Figure 7. The magnitudes of both the OH and HO_2 simulated kinetic concentrations, shown in Figure 6, were extremely sensitive to the branching fraction for $CH_3C(O)CH_2O$ formation, R2b, in the mechanism. The use of the IUPAC recommended value[66] for the branching fraction, k_{2b} / k_2 = 0.63 (± 0.20), overpredicted our experimental observations for the HO_2 and OH concentrations by a factor of ~2. Fitting the experimental data yielded a branching fraction of k_{2b} / k_2 = 0.33 (± 0.13) and dramatically reduced the discrepancies between the kinetic model and our data.

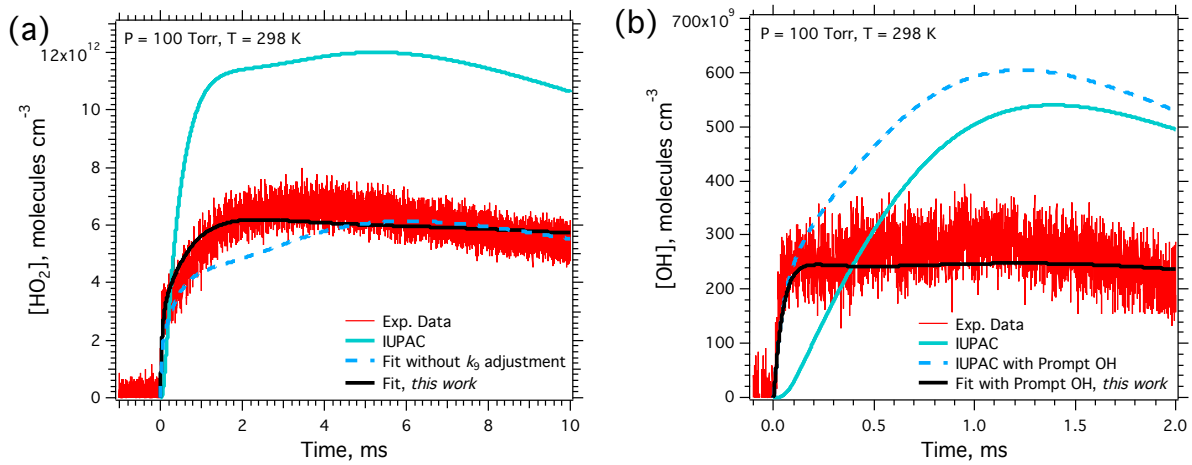

Figure 6. Experimental (red) and calculated kinetic profiles for (a) HO_2 and (b) OH for the $CH_3C(O)CH_2O_2$ self-reaction. The kinetic model (turquoise) shows the simulated concentrations using the IUPAC recommended rate parameters[66] and the results of the fit (black) shows the simulated concentrations with the parameters from this work. The dashed blue lines show (a) the fit without k_9 adjustment (see text) and (b) the model simulated with prompt OH arising from the acetonyl + O_2 reaction (see text) for comparison. The uncertainties in the experimentally

measured HO_2 and OH concentrations were ± 3.2 × 10^{10} and ± 1.4 × 10^9 molecules cm^{-3}, respectively.

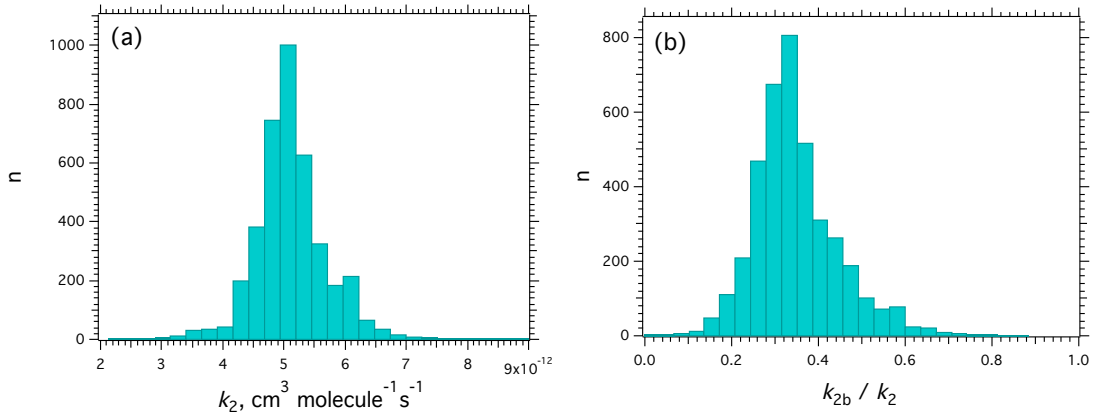

Figure 7. Histogram output from the MC simulations (4000 iterations) for (a) k_2 = (4.8 ± 0.8) × 10^{-12} cm^3 $molecule^{-1}$ s^{-1} and (b) k_{2b} / k_2 = 0.33 ± 0.13.

The fit in Figure 5 was primarily dependent on the absolute concentration of the $CH_3C(O)CH_2O$ product formation through the R2b channel as opposed to the relative product formation between R2b and the other reaction pathways as discussed in Section IIIa. Equivalent fits to that shown in Figure 6 were achieved when maintaining a branching fraction for R2b pathway of 0.33 (± 0.13) with any combined remaining branching fraction of the R2a + R2c. Therefore, our experiments cannot distinguish between the other two channels, R2a and R2c. However, the recent mass-spectrometry study by Berndt et al.[28] observed and proposed a mechanism for a third channel, R2c, for the $CH_3C(O)CH_2O_2$ self-reaction which leads to accretion product formation (ROOR) with a rate constant of 1.3 × 10^{-12} cm^3 $molecule^{-1}$ s^{-1}. Their results inferred a product branching fraction at 295 K for R2c of 0.16 based on the recommended overall k_2. Based on their rate constant for R2c and k_2 determined in this work, a larger branching fraction for the R2c accretion product channel of 0.30 was calculated.

Monitoring the HO_2 and OH concentrations constrained the fit for the rate constant and branching fractions while also providing insight to the secondary chemistry arising from R2. The secondary chemistry is complex; however, the difference in the chemical timescales for the

modeled reaction mechanism in comparison to the experimental data enabled the characterization of the experimentally observed HO_2 and OH concentrations. A possible explanation for the relationship between the time-dependent HO_2 and OH concentrations and the magnitude of the branching fraction involve the subsequent alkoxy product chemistry. Here, the $CH_3C(O)CH_2O$ product formation rapidly decomposes to the acetyl, CH_3CO, product (R8) which is oxidized to form acetyl peroxy, $CH_3C(O)O_2$ (R9a), OH (R9b) and HO_2 (R9c).[39]

$$CH_3C(O)CH_2O \rightarrow CH_3CO + CH_2O \quad \text{(R8)}$$

$$CH_3CO + O_2 \rightarrow CH_3C(O)O_2 \quad \text{(R9a)}$$

$$\rightarrow OH + \text{products} \quad \text{(R9b)}$$

$$\rightarrow HO_2 + \text{products} \quad \text{(R9c)}$$

To achieve the calculated kinetic profiles for the fits shown in Figure 6, two rate parameters had to be adjusted relative to the recommended values shown in Table 1 in addition to fitting the overall $CH_3C(O)CH_2O_2$ self-reaction kinetic parameters. First, there was a significant absence of prompt OH being formed in the calculated model at early times (<0.2 ms). Augmenting the oxygenation reaction of the alkyl group (acetonyl, $CH_3C(O)CH_2$) in the initial formation of $CH_3C(O)CH_2O_2$ to include 0.02 ± 0.01 product OH formation (R5b) affected the calculated model as shown by the dashed blue line in Figure 6b.

$$CH_3C(O)CH_2 + O_2 (+M) \rightarrow CH_3C(O)CH_2O_2 (+M) \quad \text{(R5a)}$$

$$CH_3C(O)CH_2 + O_2 (+M) \rightarrow OH + \text{products} (+M) \quad \text{(R5b)}$$

The mechanism for the proposed OH formation is not resolved and further discussion of the validity of this alkyl chemistry is discussed in section IV. Due to the timescale of the prompt OH, the inclusion of prompt OH formation mechanism did not affect the fit for the branching

fraction, k_{2b} / k_2. The second parameter that was adjusted was the rate constant k_9 corresponding to reaction between $CH_3C(O)CH_2O$ and O_2 (R10).

$$CH_3C(O)CH_2O + O_2 \rightarrow CH_3C(O)CHO + HO_2 \quad \text{(R10)}$$

This reaction was shown to affect the calculated HO_2 concentrations on the time scales between 0 – 5 ms, as shown in Figure 6a (dashed blue). Increasing the rate constant by a factor of two greatly improved the fit to the experimental data. As this rate constant is relatively small compared to the decomposition pathway (R8), this adjustment did not have a significant effect on the other observed species concentration time profiles.

IIIc. $CH_3C(O)CH_2O_2 + HO_2$: Rate Constant and Branching Fraction

Figure 8 shows a representative dataset for concentration profiles of HO_2, $CH_3C(O)CH_2O_2$, and OH arising from the cross-reaction between $CH_3C(O)CH_2O_2$ and HO_2 (R1). The simulated kinetics using the IUPAC recommended values[66] is also shown in comparison to the results of the MC simulation fits obtained in this work. Unlike the $CH_3C(O)CH_2O_2$ self-reaction study, HO_2 and OH are a primary reactant and product, respectively, and determining the branching fraction for the OH channel, R1b, is more straightforward. Figure 8a shows the HO_2 concentration time dependence, which is in excess over $CH_3C(O)CH_2O_2$ concentrations by a factor of 4 – 6. It is the least sensitive of the three species to changes in k_1 because the difference between the kinetic model with the IUPAC[66] recommended values and the fit values for the HO_2 kinetic profile arises primarily from the $CH_3C(O)CH_3$ rate enhancement coefficient for the HO_2 self-reaction (discussed in detail in Section IIId).

Figure 8b shows the $CH_3C(O)CH_2O_2$ concentration time dependence, which was monitored using UV absorption at 312 nm, and Figure 8c shows the OH concentration kinetics,

which was monitored using IR-WMS; both are compared to the IUPAC modeled and out fitted kinetics. In the cross-reaction, as in the experimental results for the $CH_3C(O)CH_2O_2$ self-reaction, the prompt OH signal at early times is observable and in our fitted kinetics is simulated as arising from R5b in the mechanism. In the presence of HO_2, there is an additional prompt OH concentration source present for the cross-reaction arising at early times from the reaction between HO_2 and Cl (R11).

$$HO_2 + Cl \rightarrow OH + ClO \qquad \text{(R11)}$$

However, the additional OH at early times from R11 does not generate enough prompt OH to fit the data. A branching fraction of 0.02 ± 0.01 for R5b again fits the prompt OH kinetics as shown in Figure 8c. The fit for the branching fraction was observable in the OH kinetics as a scaling of the OH concentrations on the timescale immediately following the prompt OH formation and was, therefore, not influenced by the inclusion of the prompt OH formation mechanism. The rate constant, k_1, and branching fraction for the OH channel, k_{1b} / k_1, were determined from the MC fitting to be $(5.5 \pm 0.5) \times 10^{-12}$ cm^3 molecule^{-1} s^{-1} and 0.30 ± 0.04, respectively. The uncertainties in our reported values were determined from a series of MC simulations as described in section IIB; a representative set of histograms for the k_1 and k_{1b} / k_1 are shown in Figure 9a and 9b, respectively. The resulting fits using these parameters are compared in Figure 8 to the model results using the currently recommended values[36, 66]: $k_1 = 9.0\ (\pm 1.0) \times 10^{-12}$ cm^3 molecule^{-1} s^{-1} and $k_{1b} / k_1 = 0.15 \pm 0.10$. The improved agreement is clearly observable.

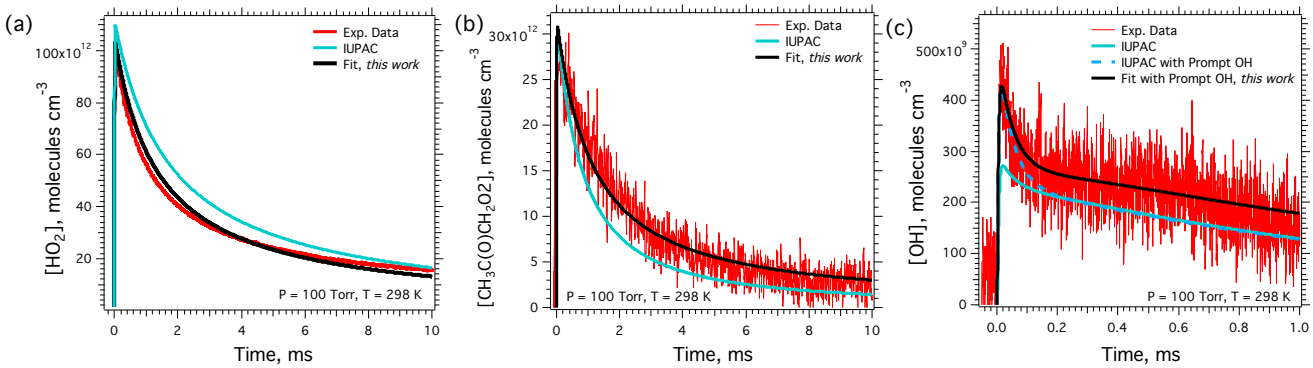

Figure 8. Experimental (a) HO_2, (b) $CH_3C(O)CH_2O_2$, and (c) OH time-dependent concentrations (red) for the HO_2 + $CH_3C(O)CH_2O_2$ reaction. Uncertainties in the measured HO_2 and OH concentrations were ± 1.6×10^{10} and 3.5×10^8 molecules cm^{-3}, respectively. The simulated concentrations using recommended rate parameters by IUPAC[66] (turquoise) are shown in all three panels. In panel (c) inclusion of the prompt OH (see text) is displayed (blue dashed) for comparison. The results of the fits of the temporal concentrations with the parameters from this work (black) are shown in all three panels

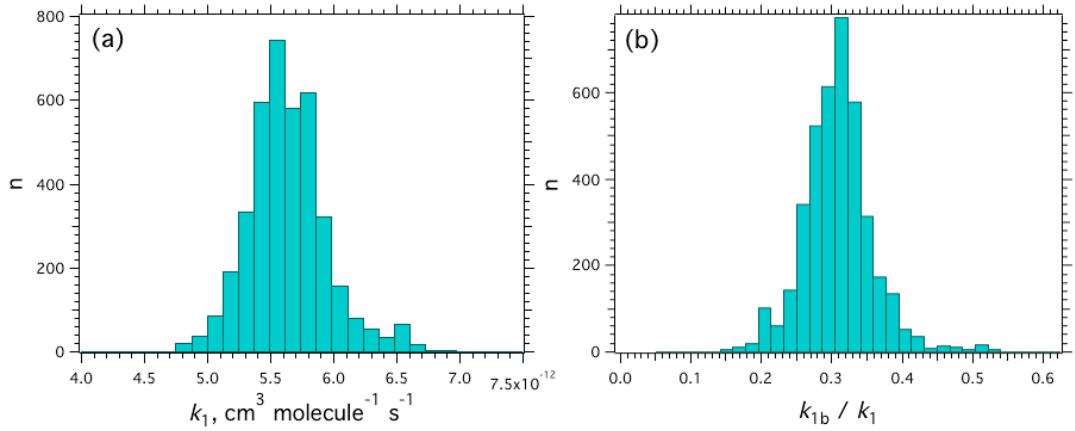

Figure 9. Histogram output from the MC simulations (4000 iterations) for (a) $k_1 = (5.5 \pm 0.5) \times 10^{-12}$ cm^3 $molecule^{-1}$ s^{-1} and (b) $k_{1b} / k_1 = 0.30 \pm 0.04$.

IIId. HO_2 + HO_2: Chaperone Effects by CH_3OH and $CH_3C(O)CH_3$

A chaperone effect, increasing the rate of the self-reaction for HO_2 (R12) via H-bonded complex formation, was observed in this work.

$$HO_2 + HO_2 \rightarrow H_2O_2 + O_2 \qquad \text{(R12)}$$

Because a change in the effective rate constant for the HO_2 self-reaction, $k_{12,obs}$, impacts the retrieved rate constants for R1 and R2,[31, 67, 68] it was necessary to assess its impact quantitatively in this study.

The chaperone rate enhancing effect by CH_3OH on R12, resulting from forming HO_2•CH_3OH has been studied previously[67-69] and is due to the increased reaction rate of R13 compared to R12.

$$HO_2 + HO_2\bullet CH_3OH \rightarrow H_2O_2 + O_2 + CH_3OH \quad \text{(R13)}$$

It was shown to be negligible at room temperature and under the concentration conditions used in this work because, in part, the equilibrium constant for complexation, K_c(R14) is small (1.0×10^{-18} cm^3 $molecule^{-1}$) at room temperature.[36]

$$HO_2 + CH_3OH \rightleftharpoons HO_2\bullet CH_3OH \quad \text{(R14)}$$

To test for the effect of CH_3OH chaperone, we conducted experiments in the absence of $CH_3C(O)CH_3$ while varying the CH_3OH concentration (see SI for details). We verify that the chaperone effect from HO_2•CH_3OH was negligible. For the purpose of this work, the JPL recommended value[36] for k_{12} (1.55×10^{-12} cm^3 $molecule^{-1}$ s^{-1}) was used.

$CH_3C(O)CH_3$ forms a strong bond with HO_2 and its chaperone effect could be significant at room temperature. Determining the effect of HO_2•$CH_3C(O)CH_3$ complexation on k_{12} is complicated by the secondary $CH_3C(O)CH_2O_2$ peroxy radical chemistry. The fraction of HO_2 complexed as HO_2•$CH_3C(O)CH_3$ was included in the kinetic mechanism. The observed rate of R12, $k_{12,obs}$, in the presence of $CH_3C(O)CH_3$ was also allowed to vary during the MC simulations for determining the cross-reaction rate (k_1) and branching fraction (k_{1b} / k_1) for R1. We found $k_{12,obs}$ to be statistically greater than the recommended value for k_{12}.

To test the possible chaperone enhancement by $CH_3C(O)CH_3$ at room temperature, a series of experiments were conducted as a function of $CH_3C(O)CH_3$ concentration with all other experimental parameters held constant. The results, shown in Figure 10, are reported as the first observation of the chaperone effect rate enhancement on k_{12} at room temperature resulting from

HO_2•$CH_3C(O)CH_3$ complexation. These results build on observations reported for lower temperatures where significant $CH_3C(O)CH_3$ chaperone enhancement was first observed.[30]

Prior to the improvements to the IRKS system for simultaneous detection of the OH product species described in Section IIa, analogous experiments were independently performed and analyzed in our laboratory that investigated the chaperone effect of $CH_3C(O)CH_3$ on the HO_2 self-reaction. In that work, only the HO_2 and $CH_3C(O)CH_2O_2$ kinetic traces were observed and analysis was done using FACSIMILE software[70] (see SI, section SVI). The lack of OH data resulted in the k_1 rate constant and k_{1b}/k_1 branching fraction parameters being less constrained compared to the results reported in sections IIIa and IIIb. The results of these early experiments are reported here for the first time, also in Figure 10, together with the present data. The $CH_3C(O)CH_3$ concentrations from the earlier experiments overlap with those studied here, between 2.1– 2.4 × 10^{16} molecule cm^{-3}, but also extend to a higher $CH_3C(O)CH_3$ (5.2 × 10^{16} molecule cm^{-3}). The two sets of data exhibit the same linear dependence of $k_{12,obs}$ with respect to $[CH_3C(O)CH_3]$. The agreement between the two datasets taken years apart and analyzed through two independent methods yields a greater confidence in the observed increased HO_2 self-reaction rate being due to a chaperone effect. In order to consolidate the earlier datasets which did not account for uncertainties in the overall mechanism rate constants used during the fits, a 4% total uncertainty was used based on the MC fitting analysis (see SVI in SI for more details).

Equation 3 is the result of the combined linear fit, with each dataset weighted by their uncertainties:

$$k_{12,obs} = k_{12} + k''_A [(CH_3)_2CO]_0 = (1.5 \pm 0.1) \times 10^{-12} + (4.0 \pm 0.2) \times 10^{-29} \times [CH_3C(O)CH_3] \quad (E3)$$

where $k''_A = (4.0 \pm 0.2) \times 10^{-29}$ cm^6 $molecule^{-2}$ s^{-1} is the chaperone enhancement coefficient for $CH_3C(O)CH_3$ at T = 298 K and the intercept, k_{12}, agrees with the JPL recommended value[36].

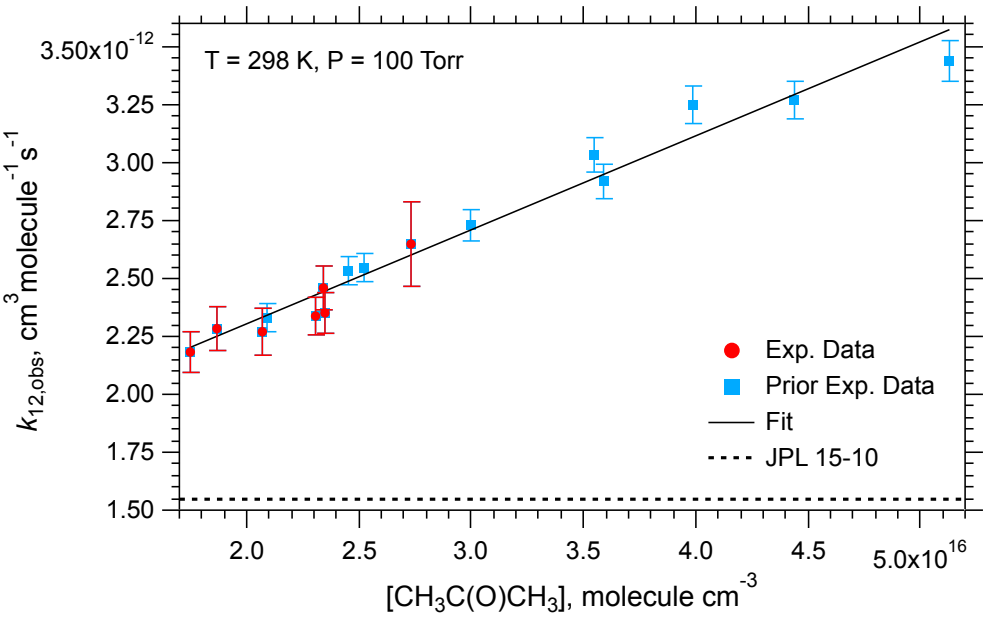

Figure 10. Experimentally determined values of $k_{12,obs}$ as a function of $CH_3C(O)CH_3$ concentration. The dashed line represents the current recommended value for $k_{12,obs}$ in the JPL Data Evaluation.[36] Exp. Data: $k_{12,obs}$ fits obtained of current data using the Monte Carlo simulations described in Section IIb. Prior Exp. Data: $k_{12,obs}$ fits of earlier data taken before IRKS modifications fit using FACSIMILE software. The overall fit was weighted by the uncertainties in each value. ($R^2 = 0.9582$).

The magnitude of the chaperone enhancement is dependent on the relative concentration of the H-bonded HO_2•$CH_3C(O)CH_3$ complex which is determined from the equilibrium constant for the formation of the complex (R15).

$$HO_2 + CH_3C(O)CH_3 \rightleftharpoons HO_2\bullet CH_3C(O)CH_3 \qquad \text{(R15)}$$

The complex enhances the self-reaction rate by R16.

$$HO_2 + HO_2\bullet CH_3C(O)CH_3 \rightarrow H_2O_2 + O_2 + CH_3C(O)CH_3 \qquad \text{(R16)}$$

The timescale for the attainment of equilibrium for R15 is much faster (< 100 μs) than the millisecond timescale of our kinetic observations. The recommended value[36] for the equilibrium constant at room temperature, $K_c(R15) = (1.4 \pm 0.84) \times 10^{-18}$ cm^3 molecule^{-1}, is extrapolated from lower temperature studies[31, 71] with the highest temperature for the $K_c(R15)$ measurement being 272 K. $K_c(R15)$ at T = 298 K can be determined directly here using the method given in Grieman

et al.[31] although it is difficult to measure because of the relatively large change in initial [HO_2] at t = 0 s caused by R4, the reaction of Cl with $CH_3C(O)CH_3$ relative to the change caused by the complex equilibrium (R15). (See SVII in SI.) We obtain K_c(R15) = (2.0 ± 0.89) × 10^{-18} cm^3 $molecule^{-1}$ (K_{eq}(R15) = 50 ± 22, standard state of 1 bar) based on a weighted average of four runs, where the uncertainty includes the propagation of all the estimated experimental errors in addition to the standard deviation from the weighted average. The directly determined value is 40% higher than the extrapolated recommended value[36], but is in agreement. For the $CH_3C(O)CH_3$ concentration range shown in Figure 10 for the early datasets (2.1 – 5.1 × 10^{16} molecules cm^{-3}), the percent complexation of HO_2•$CH_3C(O)CH_3$ ranges between 4.0 – 9.2 % at room temperature. These results as well as the rate enhancement for the HO_2 self-reaction resulting from R15 were incorporated into the MC simulations for determining k_1.

The equilibrium constant allows us to estimate the rate constant k_{16} by following the work by Christensen et al. on the HO_2 self-reaction CH_3OH enhancement.[67] Under our conditions where K_c(R15) [$(CH_3)_2CO$] << 1, and using the constants obtained from Equation 3, we obtain k_{16} from

$$k_{16} = k''_A / K_c(R15) + 2\ k_{12} = (2.0 \pm 1.0) \times 10^{-11}\ cm^3\ molecule^{-1}\ s^{-1} \quad \text{(E4)}$$

at room temperature, where most of the uncertainty arises from K_c(R15). This value is very similar to the analogous rate constant for the HO_2•CH_3OH complex which was estimated to be k_{13} = (2.1 ± 0.7) x 10^{-11} cm^3 $molecule^{-1}$ s^{-1} averaged over T = 222 – 295 K at 100 Torr and using a K_c averaged over T = 230 – 260 K.[67] Although there is no determination of the temperature dependence of this rate constant, the magnitude of k_{16} for $CH_3C(O)CH_3$ at room temperature is estimated to be the same as that for CH_3OH, k_{14}, at significantly lower temperatures where the complex formation reactions may be faster at the same pressure.

IIIe. EVALUATION OF OH GENERATION FROM THE $CH_3C(O)CH_2$ RADICAL + O_2 REACTION

To assess the potential for OH formation following O_2-addition to the $CH_3C(O)CH_2$ radical, we studied the unimolecular reaction system outlined in Figure 11 starting from the $CH_3C(O)CH_2$ radical (A1) with energetics as shown in Figure S4 (see SI). The reactions include those found to have the lowest barrier heights by Weidman et al.[72] as well as an additional H-shift following a second O_2-addition. The initial reaction is a 1,5 H-shift from the methyl group with an MC-TST calculated rate coefficient of 5.9×10^{-6} s^{-1}. The high barrier resulting in low rate coefficient for this reaction is in agreement with previous studies[17, 72-75] and has been ascribed to the strain in the TS induced by the sp^2-hybridized carbon atom reducing the flexibility.[72] This means that the 1,5 H-shift is negligible from the thermalized peroxy radical under all relevant time scales and any possible OH-recycling from reactions following this H-shift thus relies on it occurring via excess energy from the O_2-addition to the $CH_3C(O)CH_2O_2$ radical. However, in agreement with most of the previous studies,[17, 72-74] we find that the TS for the 1,5 H-shift is higher in energy than the separated $CH_3C(O)CH_2$ radical and O_2 (by 3.8 kcal mol^{-1} according to our calculations) and as shown in Figure 12, that means that the H-shift reaction does not occur via excess energy. Thus OH formation based on reactions following this 1,5 H-shift seems a highly unlikely explanation for the observed OH products and currently no explanation has been found for the experimental observations. Very recent high-level results by Weidman et al.[72] also find that formation of OH is highly unlikely from $CH_3C(O)CH_2 + O_2$ under ambient conditions. This is in agreement with our calculations which shows that this also applies to our experimental conditions and when considering the possibility of a second O_2-addition.

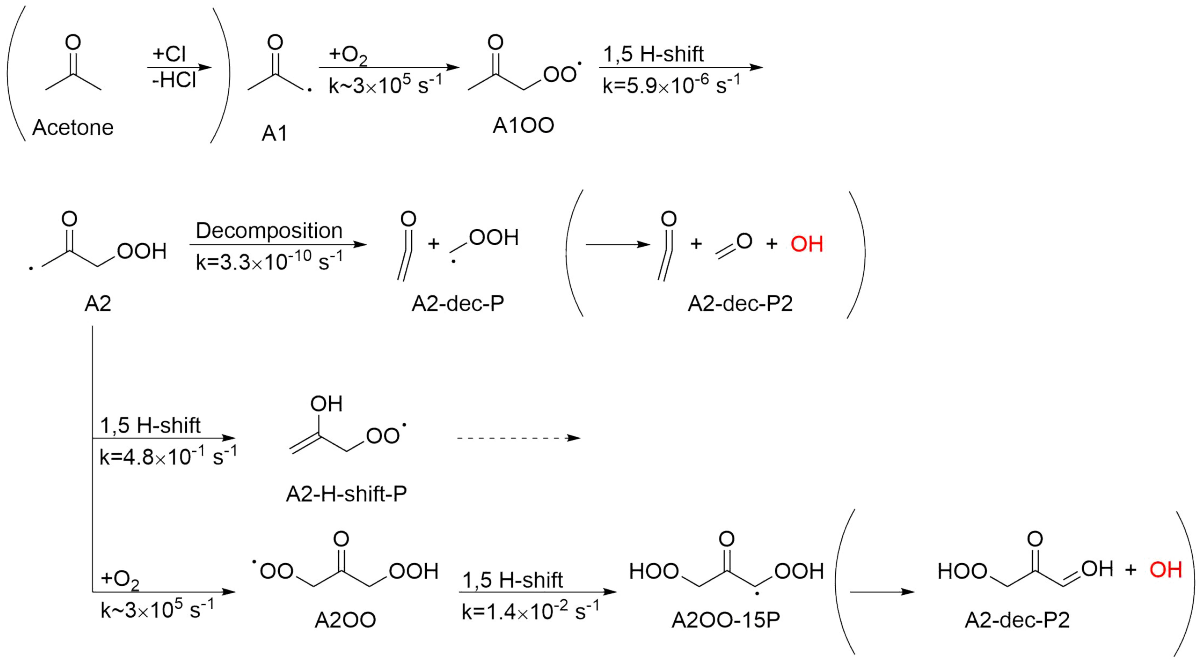

Figure 11. Overview of the reactions modelled using RRKM-ME. Reactions in parentheses are not modelled explicitly, but are assumed to occur with unity yield. MC-TST rate coefficients at 298.15 K calculated using the approach by Møller et al.[44] are given for the unimolecular reactions and estimated pseudo-first order rate coefficients for the O_2-additions are given based on the typical experimental conditions of $[O_2] = 1.6 \times 10^{18}$ molecule cm^3 and k_{5a} from Table 2.

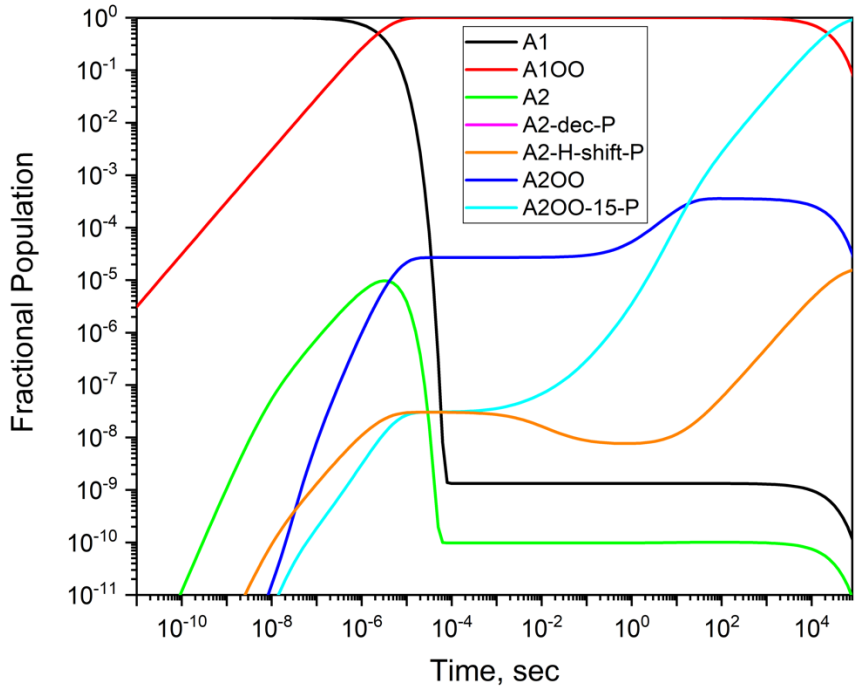

Figure 12. Time-dependent species population of the modelled system under the experimental conditions. Labels refer to the scheme outlined in Figure 11.

IV. DISCUSSION

This is the first study to measure $CH_3C(O)CH_2O_2$, HO_2, and OH simultaneously to determine the rate constants and branching fractions for the reaction between $CH_3C(O)CH_2O_2$ and HO_2 (R1), and the $CH_3C(O)CH_2O_2$ self-reaction (R2). As shown in Table 3, prior experimental studies on this system are scarce where the study by Bridier et al (1993)[21] was the sole paper to measure both rate constants for these reactions. In contrast to their work, the results presented here are not subject to the disadvantage of relying solely on UV absorption techniques, specifically the deconvolution of the UV traces with high uncertainty in the absorption cross-sections. In addition, the chaperone mechanism that we have shown to be substantial was not previously considered. Subsequent work measuring the branching fractions for R1 and R2 through detection of OH relied on the rate constants measured by Bridier et al. (1993) and, therefore, are subject to the same systematic errors. Indeed, the branching fractions reported in the literature for this cross-reaction and self-reaction ranged from 0.15 – 0.67 and 0.50 – 0.75, respectively, indicating that measurements for this system were poorly constrained. By independently re-measuring $\sigma_{CH3C(O)CH2O2}$ in a region where other species absorptions are minimal, characterizing the chaperone effects, and measuring the three species simultaneously, this work is less susceptible to the systematic errors of the previous studies.

Table 3: Summary of Experimental and Theoretical Kinetic Rate Constants and Branching Fractions for R1 and R2.

Ref. , year P (Torr), T (K)	Method	k_1	Branching Fractions, k_1^{-1}		k_2	Branching Fractions, k_2^{-1}		
			R1a	R1b		R2a	R2b	R2c
[25], 1990 760, 298	PR, UVA	-	-	-	8.3 (1.6)	-	-	-
[20], 1993 760, 298	FP, UVA	9.0 (1.0)	-	-	8.0 (2.0)	-	0.75 (0.10)	-
[19], 2004 800, 298	FTIR, HPLC, F	-	0.33 (0.13)	0.67 (0.20)	-	-	-	-
[14], 2008 700, 296	UVP, FTIR	-	-	0.15 (0.08)	-	-	-	-

[17], 2008 75–530, 298	PLP, LIF	-	-	~ 0.15	-	-	-	-
[26], 2003 765, 298	UVP, GC	-	-	-	-	-	0.50 (0.05)	-
[15], 2005 1–760, 298	CBS-QB3// B3LYP/6-311G(2d,d,p) RRKM-ME		0.79	0.21				
[18], 2012 800, 295	UVP, FTIR, HPLC	-	0.75 (0.13)	0.25 (0.13)	-	-	-	
[27], 2019 750, 297	MS	-	-	-	-	-	-	0.16‡
this work 100, 298	PLP, UVA, IR-WMS	5.5 (0.5)	0.70 (0.04)	0.30 (0.04)	4.8 (0.8)	0.37*	0.33 (0.13)	0.30†
JPL 15-10		9.0 (1.0)	-	-	-	-	-	-
IUPAC		9.0 (1.0)	0.85 (0.1)	0.15 (0.1)	8.0 (0.3)	-	0.63 (0.20)	-

Notes: Rate constants units = 10^{-12} cm^3 $molecule^{-1}$ s^{-1}. Reported uncertainties are in parentheses. PR = pulsed radiolysis; FP= flash photolysis; UVA = UV absorption spectroscopy; FTIR = Fourier transform infrared spectroscopy; HPLC = high-performance liquid chromatography; F = fluorescence detection; PLP = pulsed laser photolysis, LIF = laser induced fluorescence; UVP = UV Photolysis; GC = gas chromatography, MS = mass-spectrometric techniques, IR-WMS = infrared wavelength modulated spectroscopy, RRKM-ME = Rice-Ramsperger-Kassel-Marcus Master Equation.
‡Ratio based on the IUPAC recommended rate constant,[66] uncertainties not reported.
†Ratio based on overall rate constant, k_2, from this work.

The rate constants for both the $CH_3C(O)CH_2O_2$ reaction with HO_2 (k_1) and the $CH_3C(O)CH_2O_2$ self-reaction (k_2) are both smaller than previously reported by Bridier et al. by about 60%. A possible explanation for this systematic difference is that the UV cross-sections used in the work by Bridier et al. were up to 40 – 60% higher than those determined in this work and those found by other studies.[26, 29] A larger cross-section would result in a larger rate constant. Their method also required that the concentration time dependence of multiple species be de-convoluted from UV spectra, which is susceptible to the uncertainties arising in the absorption cross-sections from all of these species, particularly those arising from secondary chemistry (such as $CH_3(O)O_2$, CH_3O_2, and O_3, as shown in the SI). To overcome these challenges, our approach was to accurately re-measure absorption cross-section values for $CH_3C(O)CH_2O_2$, monitor [$CH_3C(O)CH_2O_2$] at a wavelength where no other species absorbs, and to simultaneously monitor key species independently using IR-WMS (for which uncertainties are lower) to better constrain the analysis.

An additional reaction mechanism that has not been considered in previous studies involving $CH_3C(O)CH_2O_2$ is the reaction between $CH_3C(O)CH_2O_2$ and OH radicals. The reaction between RO_2 and OH reaction has been observed for CH_3O_2, $C_2H_5O_2$, $C_3H_7O_2$, and $C_4H_9O_2$, but there is currently no experimental or theoretical evidence of this reaction for $CH_3C(O)CH_2O_2$.[10] The potential implications of the OH radical reaction, R17, on the rate parameter values reported in this work have been assessed by adding R17 to the overall reaction mechanism (Table 1).

$$CH_3C(O)CH_2O_2 + OH \rightarrow HO_2 + CH_3C(O)CH_2O \quad \text{(R17)}$$

An estimated rate of $(5 \pm 4) \times 10^{-11}$ cm^3 $molecule^{-1}$ s^{-1} and HO_2 product formation was used based on recent work for this class of reactions. The mean value for the rate and branching fraction for R1 were unaffected by the addition of R17 in the MC simulations. However, the uncertainty in k_1 and k_{1b} / k_1 scaled with the input uncertainty for R17. As this was highly subjective, it was not included in the final analysis of this work. Indeed, more work is necessary to understand the reaction rates and product formation channels for this class of reactions and it is beyond the scope of this work.

The branching fractions for the OH formation from R1 determined in this work fall within the large range of values observed previously.[15, 18-20] However, we observe a factor of two more OH formation for this reaction than the IUPAC recommendation.[65] This is not surprising, because the larger rate constant, k_1, used in previous analyses is directly coupled to the absolute magnitude of the [OH] time dependence. The larger rate constant affects the model by generating OH at relatively faster times where secondary species concentrations that affect the OH loss are smaller. Effectively, a higher observed [OH] would correspond to a smaller branching fraction in the model when using the larger rate constant. Although the branching fraction determined in this work is twice the currently recommended value, it is more consistent with the OH yields

from other peroxy radical + HO_2 experiments involving radicals with similar carbon number (*e.g.* $CH_3C(O)O_2$, $C_2H_5(O)O_2$, $C_3H_7(O)O_2$, and $CH_3C(O)CH_2O_2$).[36, 66, 76] In comparison to the work by Hasson et al. (2004)[20], where the branching fraction was observed to be much higher (but also with higher error) than we observe, higher concentrations of $CH_3C(O)CH_2O_2$ relative to HO_2 were used by an average factor of 2. This would make their results more susceptible to uncertainties in the $CH_3C(O)CH_2O_2$ self-reaction rate parameters which was not reinvestigated in their work.

The branching fraction for the alkoxy formation from the $CH_3C(O)CH_2O_2$ self-reaction, R2, is lower than that observed by Bridier et al, Emricha and Warneck, and the corresponding IUPAC recommended value which is an average of the two works.[21, 27, 66] The work by Bridier et al. deconvoluted overlapping UV kinetic traces as previously discussed and the work by Emricha and Warneck monitored yields of PAN formed after adding NO_2 to the system. In the latter, PAN was the only detected species and the yields were expected to be from the reaction of NO_2 with $CH_3C(O)O_2$ which are formed in the decomposition of $CH_3C(O)CH_2O$ (R2b). However, NO_2 can also react with $CH_3C(O)CH_2O_2$ to form an organic nitrate, which complicated their analysis. As a result of this complexity, they used their results to provide an upper limit on the branching fraction, which was ultimately lower than the values reported by Bridier et al. The reason for the discrepancy between our results and the literature values is uncertain; however, our direct detection of HO_2 and OH is a more constrained tracking of the $CH_3C(O)CH_2O$ pathway and reduces uncertainties in UV cross-sections and complex side chemistry resulting from nitrate formation.

All experimental data in this work showed evidence for prompt OH formation. This was modeled in the kinetic fits using the $CH_3C(O)CH_2 + O_2$ reaction (R5b). However, there is

currently no evidence for a mechanism for OH generation from this reaction based on the theoretical work reported here as well as in recent studies.[17, 72-74] The Cl + HO_2 reaction cannot resolve the discrepancy because prompt OH is observed when investigating the $CH_3C(O)CH_2O_2$ self-reaction. The possibility of contamination in the $CH_3C(O)CH_3$ sample was considered. A maximum contamination in the $CH_3C(O)CH_3$ sample (0.1%) with an absorption cross-section of 10^{-18} (λ =351 nm) under our experimental conditions leading to 100% OH product would only yield [OH] ~1×10^{11} molecule cm^{-3} when photolyzed. In the instance that the maximum potential OH concentration arising from an impurity would be achieved and, it is still not enough to explain our experimental observations which averaged higher prompt OH concentrations. Therefore, the observed prompt OH generation remains unexplained.

Finally, the chaperone effect of $CH_3C(O)CH_3$ on the HO_2 self-reaction observed in this work can be compared to a previous study at lower temperatures[31] as well as to the CH_3OH chaperone effect which has been studied more extensively.[67-69] The first observation of the $CH_3C(O)CH_3$ chaperone mechanism enhancement was described by Grieman et al.[31] at significantly lower temperatures and reported a preliminary enhancement coefficient greater than that for CH_3OH. The work presented here shows the same trend at room temperature under our concentration conditions where the enhancement coefficient due to $CH_3C(O)CH_3$ complexation with HO_2 is seen to be approximately three times greater compared to the analogous case with CH_3OH. In fact, even at room temperature it is easily observable for $CH_3C(O)CH_3$, whereas it is considered negligible for CH_3OH.

For further comparison, the analogous enhancement coefficient for H_2O at room temperature is $k''_{H2O} = (0.6 \pm 0.42) \times 10^{-29}$ cm^6 $molecule^{-2}$ s^{-1},[68] approximately an order of magnitude smaller than that observed for $CH_3C(O)CH_3$. The chaperone effect parameters for $CH_3C(O)CH_3$ are

presented in Table 4 along with those for CH_3OH for comparison. Part of the reason for the greater enhancement of the HO_2 self-reaction, for $CH_3C(O)CH_3$ compared to CH_3OH, is the larger equilibrium constant for the formation of the hydrogen-bonded complex (K_c(R15)/K_c(R14) = 2). However, the rate constants for the reactions of HO_2 with the respective hydrogen-bonded complexes appear to be approximately the same, but the temperature dependence for these values is unknown. More experimental work is needed and an opportunity for a theoretical explanation is apparent. Regardless, the increased reaction rate for the HO_2 self-reaction must be considered in laboratory studies of kinetics involving HO_2 in the presence of significant concentrations of $CH_3C(O)CH_3$, even at room temperature. At lower temperatures, particularly those relevant to the tropopause, the chaperone effect has been observed to greatly increase[31] and needs to be considered in environments containing $CH_3C(O)CH_3$. We are currently undertaking a thorough study of the temperature dependence of this effect on HO_2 and $CH_3C(O)CH_2O_2$ chemistry. It should also be noted that no acetone concentration dependence and, therefore, no chaperone dependence was found for the cross-reaction between HO_2 and $CH_3C(O)CH_2O_2$ (R1). (See S12 in the SI.)

Table 4. Parameters related to the chaperone effect that enhances the HO_2 self-reaction rate via the reaction with the H-bonded complexes formed between HO_2 and $CH_3C(O)CH_3$ (this work) or CH_3OH. Our values found for $CH_3C(O)CH_3$ at 298 K are compared to those previously found for CH_3OH.

Parameter	**HO_2•$CH_3C(O)CH_3$**	**Parameter**	**HO_2•CH_3OH**
k''_A (cm^6 $molecule^{-2}$ s^{-1})	$(4.0 \pm 0.2) \times 10^{-29}$	k''_M (cm^6 $molecule^{-2}$ s^{-1})	$(1.09\ ^{+2.7}_{-.99}) \times 10^{-29}$ [a] $(1.52 \pm 0.69) \times 10^{-29}$ [b]
K_c(R15) (cm^3 $molecule^{-1}$) (measured)	$(2.0 \pm 0.89) \times 10^{-18}$	K_c(R14) (cm^3 $molecule^{-1}$) (recommended)	1.0×10^{-18} [c]
(recommended)	$(1.4 \pm 0.84) \times 10^{-18}$ [c]		

k_{16} (cm^3 $molecule^{-1}$ s^{-1})	$(2.0 \pm 1.0) \times 10^{-11}$	k_{13} (cm^3 $molecule^{-1}$ s^{-1})	$(2.1 \pm 0.7) \times 10^{-11}$ [a,d]
Range of % (H-bonded complex)	(4.0 – 9.2)	Range of % (H-bonded complex)	(0.36 – 0.70)
$[(CH_3)_2CO]$ (molecule cm^{-3})	$(2.1 – 5.1) \times 10^{16}$	$[CH_3OH]$ (molecule cm^{-3})	$(3.8 – 7.5) \times 10^{15}$

[a]Ref. 67 [b]Ref. 68; [c]Ref. 35, no uncertainty reported; [d]Averaged over temperatures < 298 K (See text.)

V. CONCLUSIONS

This work measured the rate constants and branching fractions for the reactions between $CH_3C(O)CH_2O_2$ and HO_2, and the associated self-reactions by simultaneously and independently monitoring the time-dependent $CH_3C(O)CH_2O_2$, HO_2, and OH concentrations by UV absorption spectroscopy and infrared 2*f*-heterodyne detection. Kinetic simulations were used to fit the data and determine the uncertainties using a Monte Carlo algorithm. The capacity of this work to monitor three species independently and simultaneously greatly constrains the analysis and gives confidence in the results. Avoiding the need to deconvolve overlapping UV spectra by the use of IR kinetic spectroscopy of individual species results in a more straightforward analysis. The UV cross-sections for $CH_3C(O)CH_2O_2$ were measured for the spectral region λ = 290-320 nm and determined to be higher than the currently recommended values[36] but lower than those observed by Bridier et al.[21] The $CH_3C(O)CH_2O_2$ self-reaction rate constant is $(4.8 \pm 0.8) \times 10^{-12}$ $molecule^{-1}$ cm^3 s^{-1} and the branching fraction for alkoxy formation inferred from secondary chemistry is 0.33 ± 0.13. The rate constant is lower than the currently recommended values as is the branching fraction. It is not surprising that there is disagreement in the branching fractions considering that the previous studies for the branching fraction were not in agreement with each other and the kinetic rate was not measured in either of the two studies, but was used in their analyses. The cross-reaction between $CH_3C(O)CH_2O_2$ and HO_2 experiments resulted in a rate constant and branching fraction for OH formation of $(5.50 \pm 0.53) \times 10^{-12}$ cm^3 $molecule^{-1}$ s^{-1} and

0.30 ± 0.04, respectively. This rate constant is again smaller than the previously reported value whereas the branching fraction is larger. The higher yields of OH observed in this work are more consistent with analogous reactions[33, 36, 66, 76] and ultimately lead to less hydro peroxide product being formed from the reaction between $CH_3C(O)CH_2O_2$ and HO_2 than previously reported. To fit the experimentally observed OH profiles, a prompt OH formation pathway was necessary, but the mechanism for this remains unclear. The $CH_3C(O)CH_3$ chaperone effect had a large effect on the rate of the HO_2 self-reaction and was also required to properly fit the experimental results even at room temperature. The chaperone coefficient, k''_A (T = 298 K) = (4.0 ± 0.2) × 10^{-29} cm^6 $molecule^{-2}$ s^{-1}, and equilibrium constant, K_c(R15) = (2.0 ± 0.89) × 10^{-18} cm^3 $molecule^{-1}$, were determined and should be considered in future peroxy experiments involving HO_2 and $CH_3C(O)CH_3$.

ASSOCIATED CONTENT

Supporting Information

The supporting information contains information on the instrumental calibrations, the RRKM-ME modelling, the UV absorption measurements of secondary species, the Facsimile fitting method, determination of the K_c(15) equilibrium constant, and additional chaperone effects.

ACKNOWLEDMENTS

This research was carried out by the Jet Propulsion Laboratory, California Institute of Technology, under contract with the National Aeronautics and Space Administration (NASA), supported by the Upper Atmosphere Research and Tropospheric Chemistry Programs. The contribution of K.Z. was supported by the appointment to the NASA Postdoctoral Program at the NASA Jet Propulsion Laboratory, administered by the Universities Space Research Association under contract with NASA. The contribution from A.H. was supported in part by the National Science Foundation (NSF Grant No. CHE-1413712), and the NASA Earth and Science Fellowship (NESSF). M.D.S. was supported by the NASA Earth and Space Science Fellowship (NNX16AO36H). This research was also supported by an appointment of F.J.G. to the NASA Postdoctoral Program at the Jet Propulsion Laboratory, administered by Oak Ridge Associated Universities through a contract with NASA and a SURP grant from Pomona College for E.D. The work by HGK was funded by the Independent Research Fund Denmark. **Author contributions:** S.S. and M.O. conceived and designed the research. K.Z. conducted the experiments and performed the data analysis. F.A.F. assisted with the IRKS instrumental upgrades. C.J.P. helped with experimental planning and the model mechanism. A.O.H., F.J.G., and E.D. conducted the early experiments and F.J.G. performed the data analysis on the part of

that work presented here. M.D.S. wrote the original kinetic analysis library. K.H.M. and H.G.K. contributed the RRKM-ME and MESMER modeling work. K.Z. and F.G. wrote the paper. All authors contributed to the scientific discussion and preparation of the manuscript.

REFERENCES

1. Orlando, J. J.; Tyndall, G. S. Laboratory Studies of Organic Peroxy Radical Chemistry: An Overview with Emphasis on Recent Issues of Atmospheric Significance. *Chem. Soc. Rev.* **2012,** *41*, 6294–6317.
2. Tyndall, G. S.; Cox, R. A.; Granier, C.; Lesclaux, R.; Moortgat, G. K.; Pilling, M. J.; Ravishankara, A. R.; Wallington, T. J. Atmospheric Chemistry of Small Organic Peroxy Radicals. *J. Geophys. Res.-Atmos.* **2001,** *106*, 12157–12182.
3. Vereecken, L.; Francisco, J. S. Theoretical Studies of Atmospheric Reaction Mechanisms in the Troposphere. *Chem. Soc. Rev.* **2012,** *41*, 6259–6293.
4. Kjaergaard, H. G.; Møller, K. H.; Otkjaer, R.; Wennberg, P. O.; Crounse, J.; Xu, L.; Praske, E.; Bates, K. Atmospheric Autoxidation via Fast Peroxy Radical Hydrogen Shift Reactions. *Abstracts of Papers of the Am. Chem. Soc.* **2019,** *258*.
5. Crounse, J. D.; Nielsen, L. B.; Jorgensen, S.; Kjaergaard, H. G.; Wennberg, P. O. Autoxidation of Organic Compounds in the Atmosphere. *J. Phys. Chem. Lett.* **2013,** *4*, 3513–3520.
6. Wennberg, P.O.; Xu, L.; Crounse, J.; Møller, K.; Kjaergaard, H.G. Unimolecular Chemistry of Organic Peroxy Radicals in the Atmosphere. *Abstracts of Papers of the Am. Chem. Soc.* **2019,** *258*.
7. Møller, K. H.; Bates, K. H.; Kjaergaard, H. G. The Importance of Peroxy Radical Hydrogen-Shift Reactions in Atmospheric Isoprene Oxidation. *J. Phys. Chem. A* **2019,** *123*, 920–932.
8. Jenkin, M. E.; Valorso, R.; Aumont, B.; Rickard, A. R. Estimation of Rate Coefficients and Branching Ratios for Reactions of Organic Peroxy Radicals for Use in Automated Mechanism Construction. *Atmos. Chem. Phys.* **2019,** *19*, 7691–7717.
9. Shallcross, D. E.; Raventos-Duran, M. T.; Bardwell, M. W.; Bacak, A.; Solman, Z.; Percival, C. J. A Semi-Empirical Correlation for the Rate Coefficients for Cross- and Self-Reactions of Peroxy Radicals in the Gas-Phase. *Atmos. Environ.* **2005,** *39*, 763–771.
10. Fittschen, C. The Reaction of Peroxy Radicals with OH radicals. *Chem. Phys. Lett.* **2019**, *725*, 102-108.
11. Franco, B.; Clarisse, L.; Stavrakou, T.; Muller, J. F.; Pozzer, A.; Hadji-Lazaro, J.; Hurtmans, D.; Clerbaux, C.; Coheur, P. F. Acetone Atmospheric Distribution Retrieved From Space. *Geophys. Res. Lett.* **2019,** *46*, 2884–2893.
12. Elias, T.; Szopa, S.; Zahn, A.; Schuck, T.; Brenninkmeijer, C.; Sprung, D.; Slemr, F. Acetone Variability in the Upper Troposphere: Analysis of CARIBIC Observations and LMDz-INCA Chemistry-Climate Model Simulations. *Atmos. Chem. Phys.* **2011,** *11*, 8053–8074.
13. Fischer, E. V.; Jacob, D. J.; Millet, D. B.; Yantosca, R. M.; Mao, J. The Role of the Ocean in the Global Atmospheric Budget of Acetone. *Geophys. Res. Lett.* **2012,** *39*, L01807.
14. Khan, M. A. H.; Cooke, M. C.; Utembe, S. R.; Archibald, A. T.; Maxwell, P.; Morris, W. C.; Xiao, P.; Derwent, R. G.; Jenkin, M. E.; Percival, et al. A Study of Global Atmospheric Budget and Distribution of Acetone Using Global Atmospheric Model STOCHEM-CRI. *Atmos. Environ.* **2015,** *112*, 269–277.

15. Jenkin, M. E.; Hurley, M. D.; Wallington, T. J. Investigation of the Radical Product Channel of the $CH_3C(O)CH_2O_2 + HO_2$ Reaction in the Gas Phase. *Phys. Chem. Chem. Phys.* **2008,** *10*, 4274–4280.
16. Hasson, A. S.; Kuwata, K. T.; Arroyo, M. C.; Petersen, E. B. Theoretical Studies of the Reaction of Hydroperoxy Radicals ($HO_2\bullet$) with Ethyl peroxy ($CH_3CH_2O_2\bullet$), Acetyl peroxy ($CH_3C(O)O_2\bullet$) and Acetonyl Peroxy ($CH_3C(O)CH_2O_2\bullet$) Radicals. *J. Photochem. Photobiol. A* **2005,** *176*, 218–230.
17. Kovacs, G.; Zador, J.; Farkas, E.; Nadasdi, R.; Szilagyi, I.; Dobe, S.; Berces, T.; Marta, F.; Lendvay, G. Y. Kinetics and Mechanism of the Reactions of CH_3CO and $CH_3C(O)CH_2$ Radicals with O_2. Low-Pressure Discharge Flow Experiments and Quantum Chemical Computations. *Phys. Chem. Chem. Phys.* **2007,** *9*, 4142–4154.
18. Dillon, T. J.; Crowley, J. N. Direct Detection of OH Formation in the Reactions of HO_2 with $CH_3C(O)O_2$ and Other Substituted Peroxy Radicals. *Atmos. Chem. Phys.* **2008,** *8*, 4877–4889.
19. Hasson, A. S.; Tyndall, G. S.; Orlando, J. J.; Singh, S.; Hernandez, S. Q.; Campbell, S.; Ibarra, Y. Branching Ratios for the Reaction of Selected Carbonyl-Containing Peroxy Radicals with Hydroperoxy Radicals. *J. Phys. Chem. A* **2012,** *116*, 6264–6281.
20. Hasson, A. S.; Tyndall, G. S.; Orlando, J. J. A Product Yield Study of the Reaction of HO_2 Radicals with Ethyl Peroxy ($C_2H_5O_2$), Acetyl Peroxy ($CH_3C(O)O_2$), and Acetonyl Peroxy ($CH_3C(O)CH_2O_2$) Radicals. *J. Phys. Chem. A* **2004,** *108*, 5979–5989.
21. Bridier, I.; Veyret, B.; Lesclaux, R.; Jenkin, M. E. Flash-Photolysis Study of the UV Spectrum and Kinetics of Reactions of the Acetonylperoxy Radical. *J. Chem. Soc. Faraday Trans.* **1993,** *89*, 2993–2997.
22. Carslaw, N.; Creasey, D. J.; Harrison, D.; Heard, D. E.; Hunter, M. C.; Jacobs, P. J.; Jenkin, M. E.; Lee, J. D.; Lewis, A. C.; Pilling, M. J.; et al. OH and HO_2 Radical Chemistry in a Forested Region of North-Western Greece. *Atmos. Environ.* **2001**, *35*, 4725–4737.
23. Lelieveld, J.; Butler, T. M.; Crowley, J. N.; Dillon, T. J.; Fischer, H.; Ganzeveld, L.; Harder, H.; Lawrence, M. G.; Martinez, M.; Taraborrelli, D.; Williams, J. Atmospheric Oxidation Capacity Sustained by a Tropical Forest. *Nature* **2008,** *452*, 737–740.
24. Kubistin, D.; Harder, H.; Martinez, M.; Rudolf, M.; Sander, R.; Bozem, H.; Eerdekens, G.; Fischer, H.; Gurk, C.; Klupfel, T.; et al. Hydroxyl Radicals in the Tropical Troposphere Over the Suriname Rainforest: Comparison of Measurements with the Box Model MECCA. *Atmos. Chem. Phys.* **2010,** *10*, 9705–9728.
25. Whalley, L. K.; Edwards, P. M.; Furneaux, K. L.; Goddard, A.; Ingham, T.; Evans, M. J.; Stone, D.; Hopkins, J. R.; Jones, C. E.; Karunaharan, A.; et al. Quantifying the Magnitude of a Missing Hydroxyl Radical Source in a Tropical Rainforest. *Atmos. Chem. Phys.* **2011,** *11*, 7223–7233.
26. Cox, R. A.; Munk, J.; Nielsen, O. J.; Pagsberg, P.; Ratajczak, E. Ultraviolet-Absorption Spectra and Kinetics of Acetonyl and Acetonylperoxy Radicals. *Chem. Phys. Lett.* **1990**, *173*, 206–210.
27. Emricha, M.; Warneck, P. Branching Ratio for the Self-Reaction of Acetonyl Peroxy Radicals. *Z. Naturforsch. A* **2003,** *58*, 429–433.
28. Berndt, T.; Scholz, W.; Mentler, B.; Fischer, L.; Herrmann, H.; Kulmala, M.; Hansel, A. Accretion Product Formation from Self- and Cross-Reactions of RO_2 Radicals in the Atmosphere. *Angew. Chem. Int. Ed.* **2018,** *57*, 3820–3824.

29. Nielsen, O. J.; Johnson, M. S.; Wallington, T. J.; Christensen, L. K.; Platz, J. UV Absorption Spectra of HO_2, CH_3O_2, $C_2H_5O_2$, and $CH_3C(O)CH_2O_2$ Radicals and Mechanism of the Reactions of F and Cl Atoms with $CH_3C(O)CH_3$. *Int. J. Chem. Kinet.* **2002,** *34*, 283–291.
30. Emricha, M.; Warneck, P. Branching Ratio for the Self-Reaction of Acetonyl Peroxy Radicals. *Z. Naturforsch. A* **2003,** *58*, 429–433.
31. Grieman, F. J.; Noell, A. C.; Davis-Van Atta, C.; Okumura, M.; Sander, S. P., Determination of Equilibrium Constants for the Reaction between Acetone and HO_2 Using Infrared Kinetic Spectroscopy. *J. Phys. Chem. A* **2011,** *115*, 10527–10538.
32. Hui, A. O.; Okumura, M.; Sander, S. P. Temperature Dependence of the Reaction of Chlorine Atoms with CH_3OH and CH_3CHO. *J. Phys. Chem. A* **2019,** *123*, 4964–4972.
33. Hui, A. O.; Fradet, M.; Okumura, M.; Sander, S. P. Temperature Dependence Study of the Kinetics and Product Yields of the HO_2 + $CH_3C(O)O_2$ Reaction by Direct Detection of OH and HO_2 Radicals Using 2f-IR Wavelength Modulation Spectroscopy. *J. Phys. Chem. A* **2019**∫ *123*, 3655–3671.
34. Christensen, L. E. Laboratory Studies of Atmospherically Important Gas-Phase Peroxy Radical Reactions. Ph.D. Dissertation, California Institute of Technology 2002.
35. Smarte, M. D. *Modeling and Fitting of ALS MPIMS Kinetics*, v1.2.0; Caltech Data: 2019; https://data.caltech.edu/records/1248.
36. Burkholder, J. B.; Sander, S. P.; Abbat, J. P. D.; Barker, J. R.; Huie, R. E.; Kolb, C. E.; Kurylo, M. J.; Wilmouth, D. M.; Orkin, V. L.; Wine, P. H. *Chemical Kinetics and Photochemical Data for Use in Atmospheric Studies, Evaluation No. 18*. JPL Publication 15-10: Jet Propulsion Laboratory, Pasadena, 2015.
37. Levenberg, K. A Method for the Solution of Certain Non-Linear Problems in Least Squares. *Quart. Appl. Math.* **1944,** *2*, 164–168.
38. Marquardt, D. An Algorithm for Least-Squares Estimation of Nonlinear Parameters. *J. Soc. Ind. Appl. Math.* **1963,** *11*, 431–441.
39. Orlando, J. J.; Tyndall, G. S.; Vereecken, L.; Peeters, J. The Atmospheric Chemistry of the Acetonoxy Radical. *J. Phys. Chem. A* **2000,** *104*, 11578–11588.
40. Papadimitriou, V. C.; Karafas, E. S.; Gierczak, T.; Burkholder, J. B. $CH_3CO + O_2 + M$ (M = He, N_2) Reaction Rate Coefficient Measurements and Implications for the OH Radical Product Yield. *J. Phys. Chem. A* **2015,** *119*, 7481–7497.
41. Jenkin, M. E.; Cox, R. A.; Emrich, M.; Moortgat, G. K. Mechanisms of the Cl-Atom-Initiated Oxidation of Acetone and Hydroxyacetone in Air. *J. Chem. Soc. Faraday Trans.* **1993**, *89*, 2983–2991.
42. Jenkin, M. E.; Hurley, M. D.; Wallington, T. J. Investigation of the Radical Product Channel of the $CH_3C(O)O_2 + HO_2$ Reaction in the Gas Phase. *Phys. Chem. Chem. Phys.* **2007,** *9*, 3149–3162.
43. Veyret, B.; Lesclaux, R.; Rayez, M. T.; Rayez, J. C.; Cox, R. A.; Moortgat, G. K. Kinetics and Mechanism of the Photooxidation of Formaldehyde. 1. Flash-Photolysis Study. *J. Phys. Chem.* **1989,** *93*, 2368–2374.
44. Møller, K. H.; Otkjaer, R. V.; Hyttinen, N.; Kurten, T.; Kjaergaard, H. G. Cost-Effective Implementation of Multiconformer Transition State Theory for Peroxy Radical Hydrogen Shift Reactions. *J. Phys. Chem. A* **2016,** *120*, 10072–10087.
45. Halgren, T. A. Merck Molecular Force Field. 1. Basis, Form, Scope, Parameterization, and Performance of MMFF94. *J. Comput. Chem.* **1996,** *17*, 490–519.
46. Spartan '18. *Wavefunction Inc., Irvine, CA* **2018**.

47. Lee, C. T.; Yang, W. T.; Parr, R. G. Development of the Colle-Salvetti Correlation-Energy Formula into a Functional of the Electron-Density. *Phys. Rev. B* **1988,** *37*, 785–789.
48. Hehre, W. J.; Ditchfield, R.; Pople, J. A. Self-Consistent Molecular-Orbital Methods.12. Further Extensions of Gaussian-Type Basis Sets for Use in Molecular-Orbital Studies of Organic-Molecules. *J. Chem. Phys.* **1972,** *56*, 2257–2261.
49. Clark, T.; Chandrasekhar, J.; Spitznagel, G. W.; Schleyer, P. V. Efficient Diffuse Function-Augmented Basis Sets for Anion Calculations. Iii. The 3-21+G Basis Set for First-Row Elements, Li-F. *J. Comput. Chem.* **1983,** *4*, 294–301.
50. Frisch, M. J.; Trucks, G. W.; Schlegel, H. B.; Scuseria, G. E.; Robb, M. A.; Cheeseman, J. R.; Scalmani, G.; Barone, V.; Petersson, G. A.; Nakatsuji, H.; et al. Gaussian 16 Revision C.01. *Gaussian Inc. Wallingford CT.* **2016**.
51. Frisch, M. J.; Pople, J. A.; Binkley, J. S. Self-Consistent Molecular-Orbital Methods. 25. Supplementary Functions for Gaussian-Basis Sets. *J. Chem. Phys.* **1984,** *80*, 3265–3269.
52. Becke, A. D. Density-Functional Thermochemistry. 3. The Role of Exact Exchange. *J. Chem. Phys.* **1993,** *98*, 5648–5652.
53. Otkjær, R. V.; Møller, K. H. Removal of Duplicate Conformers. *https://github.com/TheKjaergaardGroup/Removal-of-Duplicate-Conformers.*
54. Chai, J. D.; Head-Gordon, M. Optimal Operators for Hartree-Fock Exchange from Long-Range Corrected Hybrid Density Functionals. *Chem. Phys. Lett.* **2008,** *467*, 176–178.
55. Dunning, T. H., Gaussian-Basis Sets for Use in Correlated Molecular Calculations. 1. The Atoms Boron Through Neon and Hydrogen. *J. Chem. Phys.* **1989,** *90*, 1007–1023.
56. Kendall, R. A.; Dunning, T. H.; Harrison, R. J. Electron-Affinities of the 1st-Row Atoms Revisited- Systematic Basis-Sets and Wave-Functions. *J. Chem. Phys.* **1992,** *96*, 6796–6806.
57. Dunning, T. H.; Peterson, K. A.; Wilson, A. K. Gaussian Basis Sets for Use in Correlated Molecular Calculations. X. The Atoms Aluminum Ahrough Argon Revisited. *J. Chem. Phys.* **2001**, *114*, 9244–9253.
58. Werner, H. J.; Knizia, G.; Manby, F. R. Explicitly Correlated Coupled Cluster Methods with Pair-Specific Geminals. *Mol. Phys.* **2011,** *109*, 407–417.
59. Werner, H. J.; Knowles, P. J.; Knizia, G.; Manby, F. R.; Schutz, M. Molpro: A General-Purpose Quantum Chemistry Program Package. *Wiley Interdisciplinary Reviews-Computational Molecular Science* **2012,** *2*, 242–253.
60. Adler, T. B.; Knizia, G.; Werner, H. J. A Simple and Efficient CCSD(T)-F12 Approximation. *J. Chem. Phys.* **2007,** *127,* 221106.
61. Knizia, G.; Adler, T. B.; Werner, H. J. Simplified CCSD(T)-F12 Methods: Theory and Benchmarks. *J. Chem. Phys.* **2009,** *130*, 054104.
62. Peterson, K. A.; Adler, T. B.; Werner, H. J. Systematically Convergent Basis Sets for Explicitly Correlated Wavefunctions: The Atoms H, He, B-Ne, and Al-Ar. *J. Chem. Phys.* **2008**, *128* (8).
63. Watts, J. D.; Gauss, J.; Bartlett, R. J. Coupled-Cluster Methods with Noniterative Triple Excitations for Restricted Open-Shell Hartree-Fock and Other General Single Determinant Reference Functions–Energies and Analytical Gradients. *J. Chem. Phys.* **1993**, *98*, 8718–8733.
64. Glowacki, D. R.; Liang, C. H.; Morley, C.; Pilling, M. J.; Robertson, S. H. MESMER: An Open Source Master Equation Solver for Multi-Energy Well Reactions. *J. Phys. Chem. A* **2012,** *116*, 9545–9560.
65. Eckart, C. The Penetration of a Potential Barrier by Electrons. *Phys. Rev.* **1930,** *35*, 1303–1309.

66. Atkinson, R.; Baulch, D. L.; Cox, R. A.; Crowley, R. F.; Hampson, R. F.; Hynes, M.E.; Jenkin, M. E.; Rossi, M. J.; Troe, J.; IUPAC Subcommittees, Evaluated Kinetic and Photochemical Data for Atmospheric Chemistry: Volume II – Gas Phase Reactions of Organic Species. *Atmos. Chem. Phys.* **2006,** *6*, 3625–4055.
67. Christensen, L. E.; Okumura, M.; Hansen, J. C.; Sander, S. P., Experimental and Ab Initio Study of the HO_2•CH_3OH Complex: Thermodynamics and Kinetics of Formation. *J. Phys. Chem. A* **2006,** *110*, 6948–6959.
68. Tang, Y. X.; Tyndall, G. S.; Orlando, J. J. Spectroscopic and Kinetic Properties of HO_2 Radicals and the Enhancement of the HO_2 Self Reaction by CH_3OH and H_2O. *J. Phys. Chem. A* **2010,** *114*, 369–378.
69. Stone, D.; Rowley, D. M. Kinetics of the Gas Phase HO_2 Self-Reaction: Effects of Temperature, Pressure, Water and Methanol Vapours. *Phys. Chem. Chem. Phys.* **2005**, *7*, 2156–2163.
70. Curtis, A. R.; Sweetenham, W. P. FACSIMILE/CHEKMAT, H015 ed, v. 4.1.41. *MCPA Software: Harwell, Oxfordshire, U.K.* **1987**.
71. Dillon, T. J.; Pozzer, A.; Vereecken, L.; Crowley, J. N.; Lelieveld, J. Does Acetone React with HO_2 in the Upper-Troposphere? *Atmos. Chem. Phys.* **2012,** *12*, 1339–1351.
72. Weidman, J. D.; Turney, J. M.; Schaefer, H. F. Energetics and Mechanisms for the Acetonyl Radical + O_2 Reaction: An Important System for Atmospheric and Combustion Chemistry. *J. Chem. Phys.* **2020,** *152*, 114301.
73. Kuwata, K. T.; Hasson, A. S.; Dickinson, R. V.; Petersen, E. B.; Valin, L. C. Quantum Chemical and Master Equation Simulations of the Oxidation and Isomerization of Vinoxy Radicals. *J. Phys. Chem. A* **2005,** *109*, 2514–2524.
74. Hassouna, M.; Delbos, E.; Devolder, P.; Viskolcz, B.; Fittschen, C. Rate and Equilibrium Constant of the Reaction of 1-Methylvinoxy Radicals with O_2: $CH_3COCH_2 + O_2 \rightarrow CH_3COCH_2O_2$. *J. Phys. Chem. A* **2006,** *110*, 6667–6672.
75. El-Nahas, A. M.; Simmie, J. M.; Navarro, M. V.; Bozzelli, J. W.; Black, G.; Curran, H. J. Thermochemistry and Kinetics of Acetonylperoxy Radical Isomerisation and Decomposition: A Quantum Chemistry and CVT/SCT Approach. *Phys. Chem. Chem. Phys.* **2008,** *10*, 7139–7149.
76. Winiberg, F. A. F.; Dillon, T. J.; Orr, S. C.; Gross, C. B. M.; Bejan, I.; Brumby, C. A.; Evans, M. J.; Smith, S. C.; Heard, D. E.; Seakins, P. W. Direct Measurements of OH and Other Product Yields From the $HO_2 + CH_3C(O)O_2$ Reaction. *Atmos. Chem. Phys.* **2016,** *16*, 4023–4042.

TOC Graphic: